 doi:10.20944/preprints202204.0139.v1

Article

Functionally Graded Material Fabricated by Powder-based Laser Directed Energy Deposition: From Conventional to Complex Concentrated Alloys

Kun Li, Xin Wang and Wei Xiong*

Physical Metallurgy and Materials Design Laboratory, Department of Mechanical Engineering and Materials Science, University of Pittsburgh, Pittsburgh, PA 15261, USA
* Correspondence: Corresponding Author, Email: weixiong@pitt.edu

Abstract: Directed energy deposition (DED) is an efficient method to fabricate functionally graded materials (FGMs) with gradient composition and complex structures, allowing for local tailoring of properties instead of the costly need for extraneous welds and joints. In this study, a FGM from stainless steel to Inconel alloy was successfully fabricated using the powder-based laser DED. A very refined grain structure has been observed in at the composition with 75 wt.% Inconel alloy content, which also exhibits the highest (entropy). For the first time, the post heat treatments, microstructure and aging precipitation behaviors of FGMs were systematically studied via experimental characterization and computation, to elucidate their effects on the gradient smoothing and mechanical properties. The diffusion and segregation of Ni, Nb and Ti elements underly the transformation mechanism between Laves, δ, γ′ and γ′′ phases during precipitation. Homogenization on FGMs not only eliminates the heterogeneity inherited from the AM process, but also provides a practical way to smoothen the gradient on composition and microstructure for the eventual good gradient properties. It has a direct influence on the following precipitation behaviors in the FGM, which highly relies on the diffusion degree of the elements in the matrix and grain boundaries. The high-throughput thermodynamic modeling and kinetic modeling were exploited to evaluate the experimental microstructure and address computational uncertainty using different thermodynamic conditions and databases, which enables an accelerated design through local tailoring of process-structure-property relationships to develop new functional materials.

Keywords: Directed energy deposition; functionally graded materials; precipitation; high-throughput design

1. Introduction

As driven by the need of lightweight and cost-effective structures in the current society, dissimilar metal joints with multi-materials are highly demanded for aerospace, transportation, bioengineering, nuclear power generation, navigation and military fields [1-6]. However, dissimilar joints are prone to fail because of unexpected distortion and high gradient of residual stresses at large scales stemming from the sharp changes in chemical composition, microstructure and properties across the joint interfaces [7-15].

 doi:10.20944/preprints202204.0139.v1

Functional graded materials (FGMs) can overcome these difficulties with their continuous development since they were first conceived of in 1980s, which possess spatially varying properties with gradual transitions in chemical compositions or structures [16-20]. They also benefit basic material science by providing a new method for combinatorial alloy design and computational modeling validation [21-23].

To create FGMs with optimized stress profiles and excellent formability, additive manufacturing (AM) with a layer-wise synthesis is currently among the most dynamic developing trends to replace the traditional manufacturing methods including chemical and physical vapor deposition (CVD/PVD), plasma spray, powder metallurgy, welding processes (e.g. fusion and solid state welding) and centrifugal casting methods [24-33]. Currently, metallic material AM can be classified with two major processes: Powder Bed Fusion (PBF) and Direct Energy Deposition (DED). Compared with PBF, the DED method is more suitable to create a gradient structure due to more flexibility in the ability to change the melt pool size and powder/wire composition [33-35]. Moreover, the discrete nature of DED provides the potential for geometrically complex components without any extra supports [35-37]. The laser-based DED with the powder feedstock, also well known as Laser Engineered Net Shaping (LENS), is a compelling method in the additive manufacturing of FGMs because of the flexibility in control space and non-requirement of atmosphere vacuum compared with the electron beam DED [34,38,39].

In recent years, the primary focus of additive manufacturing of FGMs has largely been devoted toward exploring the alloy compatibility and joining possibility. The challenges associated with joining different types of alloys are comprehensively learned. They spread widely in the aspects of element incompatibilities, intermetallic formation and solubility limitations, thermal property mismatch, phase transformation and species migration, unwanted inclusions and so on, which would cause serious segregations, brittle phases, large residual stresses, distortions, cracks and failure of joining in the non-equilibrium state alloy components [40-48]. In addition, dilution as a nature of fusion processes, is another stubborn problem if it is not well controlled, which consequently resulting in issues ranging from detrimental phases to hot cracking [49-55]. To date, many researchers studied different FGMs using DED process. Ti-based and Ni-based FGMs have been widely exploited because of their high strength to weight ratio, high strength and corrosion resistance at extreme conditions, including Ti6Al4V/stainless steel (304 or 316), Ti6Al4V/TiC, Ti6Al4V/Invar, Ti6Al4V/Mo, Ti6Al4V/Inconel 718, and Ti/TiC [56-63]. Meanwhile, Fe-based FGMs are also extensively studied, especially for 316(L) and 304 stainless steels due to their low cost and high corrosion resistance, which covers 316L/Stellite 12, 316L/Inconel 718, 316L/NiCr, 316L/Ferritic steel, 316L/Fe_3Al, and 304/Inconel 625 [64-70]. It is obvious that Ti-based and Ni-based alloys and stainless steels are the attractive and favorable candidates for FGMs additive manufacturing. Domack et al [62]. studied the deposition performance for an FGM from Ti6Al4V titanium alloy to Inconel 718 with nearly continuous composition grade using the laser DED. The deposited samples exhibited coarse dendritic microstructures and significant elemental segregation with macroscopic cracking occurred for composition greater than 60vol.% Inconel 718, because

 doi:10.20944/preprints202204.0139.v1

of their different coefficients of thermal expansion (CTE) [33, 71] and brittle phases easily formed in Ti and Ni alloys [47,60]. Bobbio and Reichardt et al. [40,56] synthesized an FGM by DED consisting of Ti6Al4V and SS 304L stainless steel with V as a transition material. The distinct changes in compositions, phases and hardness across gradient were thoroughly exhibited. The cracks occurred in the SS 304L/V transition range from 50vol.% to 75%vol.% V because of the intermetallic phases [56]. Li. et al [57] proposed a successful FGM consisting of Ti6Al4V and SS316. The formation of intermetallic phases was avoided by introducing a transitional composition Ti6Al4V→V→Cr→Fe→SS316. Moreover, Inconel 718 and 316 stainless steel are two preferred materials for a critical high-integrity joints in nuclear and aerospace industries [37,72,73]. Shah et al. [66] studied the parametric behavior of an FGM wall fabricated using laser DED between these two materials. The increase in the heat input accelerated the grain growth, reducing the hardness. However, post heat treatments are rarely studied in the existing literature, which are usually required for the precipitation-hardening alloys to achieve the final mechanical properties for industrial uses [72,74,75]. In addition, post heat treatments are effective to relieve residual stress, eliminate the non-equilibrium phases and heterogeneous microstructure coming from the nature of additive manufacturing [76-79]. Furthermore, the proper post homogenization or solution heat treatments are also a promising way to smooth the gradients in composition and microstructure.

In this work, successful builds of FGM bulks from 316 stainless steel (SS316) to Inconel 718 superalloy (IN718) were achieved using the powder-based laser DED. The element composition, microstructure and mechanical properties in as-deposited FGMs were evaluated. A potential composition for novel alloy design was found using this additive manufacturing FGM as a combinatorial alloy development. The post heat treatments including homogenization and aging on the FGMs were for the first time studied to systematically elucidate their effects on the gradient smoothing and aging precipitation behaviors. The CALPHAD-based (CALculation of PHAse Diagrams) high-throughput modeling was performed to predict and compare the phases observed in the experiments. Using the different thermodynamic conditions created from post heat treatments, the thermodynamic modeling databases were evaluated via experimental characterization. This work performs a comprehensive study in deep on the microstructure evolution, gradient smoothing, precipitation behaviors and thermodynamic modeling of the FGMs, which provides a fundamental guidance for further development on FGMs.

2. Experiments and modeling

2.1. Materials and experimental design

The gradient components were fabricated on a substrate plate of stainless steel 316L (SS316L) using a directed energy system (Optomec LENS® 450 System) embedded with a Nd:YAG laser, as schematically shown in Fig. 1. IN718 and SS316 powders (Praxair Surface Technologies Inc) with particle size range of 45~125 μm (mesh size -120/+325) were used into two feeders for LENS processing. The materials compositions are noted in Table 1. Through the initial attempts, the building parameters were chosen and

Preprints (www.preprints.org) | NOT PEER-REVIEWED | Posted: 15 April 2022 doi:10.20944/preprints202204.0139.v1

adjusted depending on the height and width of melt pools of two different alloys. After parameter optimization on block builds, the graded alloys samples are built using a laser power of 300 W, a scan speed of 5 mm/s, a layer thickness of 0.25 mm and a hatch spacing of 0.75 mm with a scan pattern of 90° between each layer, which is illustrated as scan direction 1 (S1) and 2 (S2) in Fig. 1. The LENS system is flexible to deposit powders with variable fraction of powders by controlling the feed rates. Through our baggie test and taking into consideration of the acceleration and deceleration of powders, the weight percent of each powder can be accurately alternated by the feed rate of each nozzle. In this work, the FGMs were built from pure SS316 to pure IN718 with an increased alloy gradient of 25 wt.%. Each composition of the material was applied to deposit four layers.

Table 1. The compositions of powders and substrate plate (wt.%)

Material	C	Ni	Cr	Fe	Nb	Ti	Al	Co	Mo	Mn	Si	Others
In 718	0.04	53.35	18.98	18.14	5.09	0.94	0.41	0.03	2.93	0.01	0.06	Bal.
SS 316	0.08	12	17	67.97	—	—	—	—	2	1	—	Bal.
Substrate 316L	0.004	12	17	66.75	—	—	—	—	2.5	1.5	0.75	Bal.

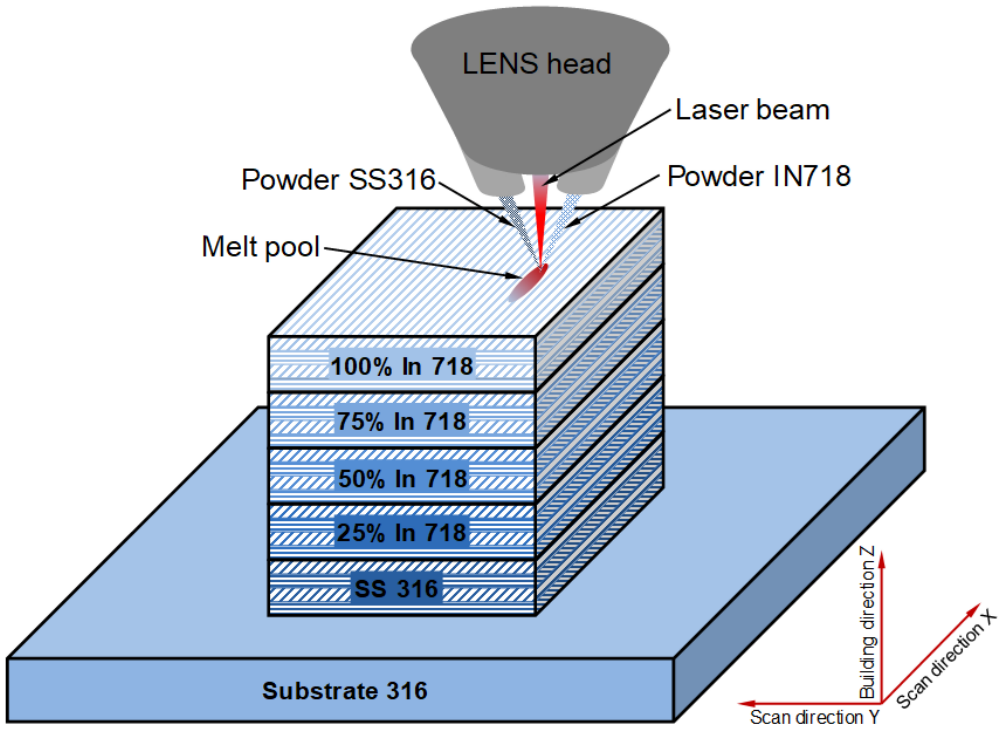

Figure 1. Schematic of laser-based directed energy deposition (DED) for the functional graded material (FGM) building from SS316 to IN718.

Several final deposited FGMs were successfully obtained with good forming control, as shown in Fig. 2a. Certain blocks were cut into several samples along A-A cross section parallel to building direction (BD) by wire electric discharge machine for microstructure and mechanical characterization (Fig. 2b). Several alloy pieces with composition gradient were encapsulated into vacuumed quartz tubes filled with pure argon for

Preprints (www.preprints.org) | NOT PEER-REVIEWED | Posted: 15 April 2022 doi:10.20944/preprints202204.0139.v1

post heat treatments. Then some of the samples were directly subjected to aging at 718ºC for 15 h, followed by water quenching. Other bunch of samples were carried out with post homogenization at 1200ºC for 1 hour (1-h) and 7 days (7-d) followed by water quenching, respectively. Afterwards, they were all subjected to the same aging process as stated above. The samples were mounted and polished with standard metallographic methods, then etched with aqua regia (1 vol.% nitric acid + 3 vol.% hydrochloride acid) for 30 s. Microstructure as a function of location were observed using optical microscope (OM, Zeiss Smartzoom5) and scanning electron microscope (SEM, Zeiss Sigma 500 VP). Electron back-scattered diffraction technique (EBSD) were performed using the FEI Scios Dual Beam System to investigate the grain evolution, with a scanning step size of 0.08 μm. High resolution SEM combined with energy dispersive spectroscopy (EDS) were carried out to elucidate phase morphologies and transformations as a function of composition. The chemical compositions and phases in the aged FGMs were analyzed by electron probe microanalyzer (EPMA). Hardness of samples was evaluated by Vickers microhardness auto-tester (LECO LM800) with a load of 300 g and a dwell time of 10 s. a minimum of five measurements were taken for each location on the polished samples with avoiding the pores.

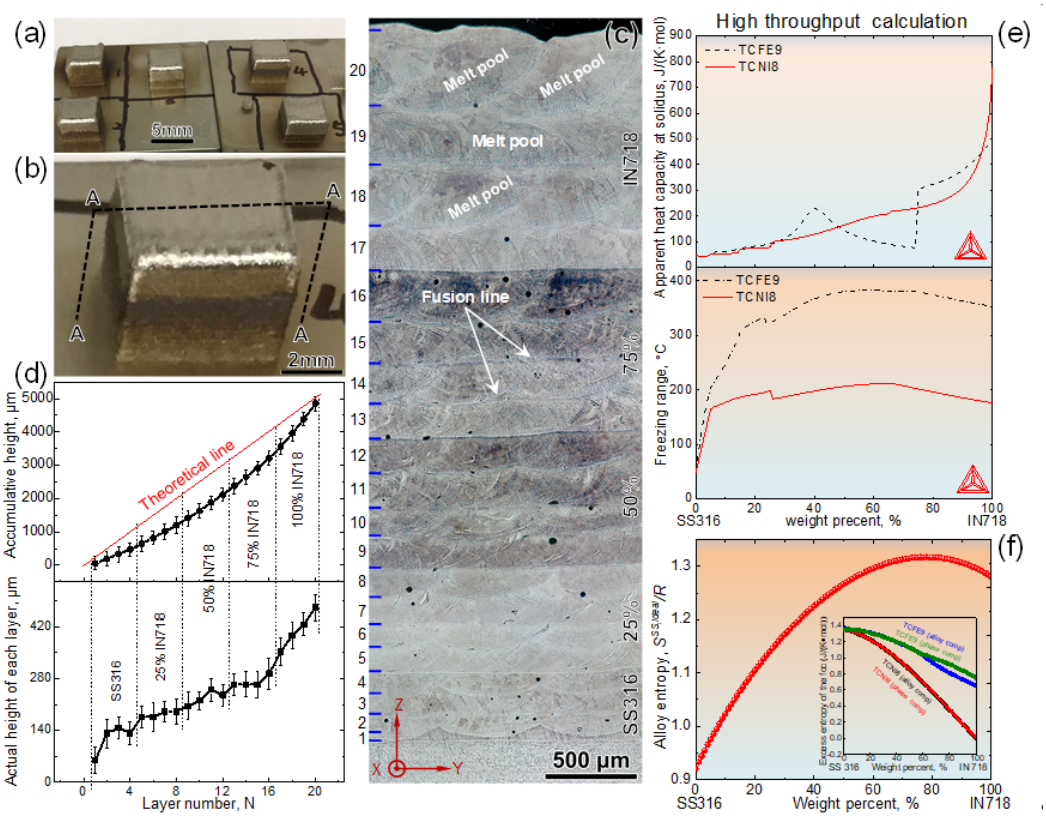

Figure 2. The successful building of FGMs from SS316 to IN718: (a) final FGM blocks, (b) the studied FGM block showing cross section A-A of sample slicing, (c) overall OM morphologies of the FGM along cross section A-A, (d) layer height distribution statistically extracted from (c), (e) high throughput calculation of physico-chemical characteristics using thermodynamic modeling and (f) high throughput calculation of alloy entropy as a function of composition.

Preprints (www.preprints.org) | NOT PEER-REVIEWED | Posted: 15 April 2022 doi:10.20944/preprints202204.0139.v1

2.2. High-throughput model prediction of phase stability

As the microstructure in FGMs by AM and post heat treatments contains stable and unstable phases under both equilibrium and nonequilibrium conditions resulting from the rapid cooling and solidification, steep thermal gradients and cyclic reheating from multiple laser passes and post heating conditions, a comprehensive study of phases in this FGM were systematically performed using CALPHAD-based modeling and Scheil modeling to predict the phases and help microstructural analyses. More compelling, TC-Python interface in Thermo-Calc was applied to understand the phase stability along the composition gradient developed between SS316 and IN718. The physico-chemical properties, phase evolution at different temperatures as a function of composition were calculated to provide an entire insight into the relationship between phases, mechanical properties, build defects, and porosity formation. In addition, in order to predict the homogenization process at 1200°C, the diffusion simulation was performed using the DICTRA (DIffusion Controlled TRAsformations) module in the Thermo-Calc software package based on TCFE9 and TCNI8 thermodynamic databases appended with MOBFE4 and MOBNI4 mobility databases [80].N

Because this FGM was developed from SS316 steel to IN718 nickel-based superalloy, the Thermo-Calc databases of TCFE9 and TCNI8 [81] were both used to improve the prediction of phase formations. For example, the equilibrium and nonequilibrium phases calculated from TCFE9 and TCNI8 are of big differences for a composition of 50wt.% IN718 alloy, as shown in Fig. 3. The δ phase was suspended in the calculation of TCNI8 to make sure the presence of γ′ and γ′′ phases, which was adopted for all the following simulations in TCNI8. In the case of equilibrium simulation, MX, Laves and σ phases occur in both TCFE9 and TCNI8 databases, while the secondary phases of γ′ and γ′′ formed in TCNI8 are totally different from $NbNi_3$ and Ni_3Ti phases occurring in TCFE9 (Figs. 3a1 and 3b1). Nonetheless, The Laves phase calculated from TCNI8 is the primary phase in the nonequilibrium simulation rather than the $NbNi_3$ phase calculated from TCFE9 (Figs. 3a2 and 3b2). These discrepancies between different databases, equilibrium and nonequilibrium simulations need to be combined to evaluate the phase predictions in this compositionally gradient material fabricated by the DED process and post heat treatments. Using this compatible approach of high-throughput thermodynamic modeling, the prediction and quantification of solidification and phase transformations were studied in depth to leverage the link between thermodynamic modeling and experimental characterization, then further guide the experimental design for FGMs.

Preprints (www.preprints.org) | NOT PEER-REVIEWED | Posted: 15 April 2022 doi:10.20944/preprints202204.0139.v1

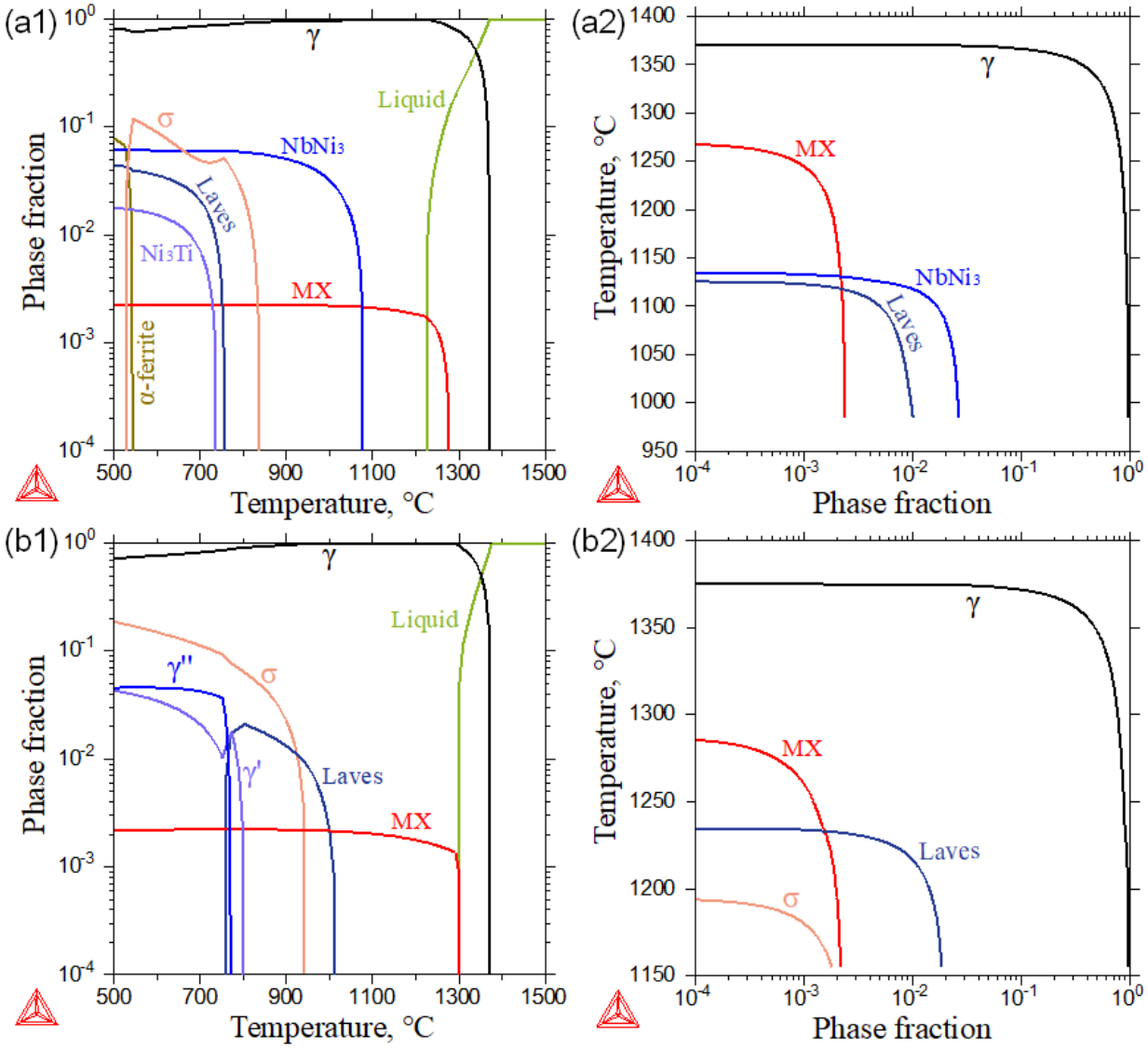

Figure 3. Thermodynamic predictions for the FGM component with the composition of 50wt.% IN718: (a) phase fraction vs. temperature (a1) and nonequilibrium simulation using the Scheil-Gulliver model (a2) using TCFE9 database, (b) phase fraction vs. temperature (b1) and nonequilibrium simulation using the Scheil-Gulliver model (b2) using TCNI8 database.

3. Results and discussion

3.1. FGM building and control

3.1.1. Macro-morphologies

The overall morphologies of as deposited FGMs were revealed in Fig. 2. There were no cracks and big forming distortions in these FGM blocks by our in-house processing control. As illustrated in Fig. 2c, the melt pools and fusion lines between each laser pass are clear to see. 20 layers were built up with five compositional gradients, i.e., pure SS316, 25wt.% IN718, 50wt.% IN718, 75wt.% IN718 and 100wt.% IN718. However, each layer has different actual layer height (H_L), which is increasing gradually as the FGM builds up (Fig. 2d). Especially when the composition is approaching to IN718, the H_L

Preprints (www.preprints.org) | NOT PEER-REVIEWED | Posted: 15 April 2022 doi:10.20944/preprints202204.0139.v1

increases rapidly. The accumulative height of layers (H_A) is non-linear and deviated from the theoretical line of ideal case, because of this mismatch between the actual layer height and the set layer thickness. However, the total built height (H_T) was well controlled at around 5 mm. The increase of H_L can be explained by the changes in the absorption of laser energy and heat accumulation of each layer. Figure 2e presents the computed apparent heat capacity at solidus (C_P^S) of the FGM as a function of composition. It can be seen that the C_P^S has an increasing trend with the weight percent of IN718 increasing in both TCFE9 and TCNI8 simulations. Whereas, it varies seriously in TCFE9 when IN718 is greater than 25wt.%. When the composition is higher than 75wt.% IN718, the C_P^S calculated from both TCFE9 and TCNI8 simulations increases sharply, which shows a good accordance with the H_L. It indicates the closely direct influence of the C_P^S of materials on the H_L. Because the apparent heat capacity is closely related to the heat absorption [82-84], the increased heat capacity represents the higher ability of heat absorption from laser energy. This causes that the powders with high Ni content are easier to melt and get a higher melt volume during laser printing. Meanwhile, due to the higher heat capacity, the built component near to the IN718 side has a higher heat accumulation which can be incorporated into the next laser pass for melting to further increase the H_L. This elucidation points out the significance of laser energy and heat accumulations when fabricating FGMs with big difference in heat capacity of materials.

Another notable phenomenon is the pores in the FGM are few (the print density is higher than 98.5% using the measurement of Archimedes method). Most of them forms near the fusion lines of melt pools (Fig. 2c). It is known to all that the formation of porosity in traditional process is related to its nucleation and escape from melt pool. The nucleation of porosity is closely attributed to the stability of melt pool, and the escape ability of porosity is attributed to the solidification time that depends on the temperature range between liquidus and solidus (well known as freezing range, which is also an indicator for the hot cracking and weldability). The freezing range as a function of continuous gradient composition are computed from thermodynamic databases, as presented in the downside of Fig. 2e. It shows that the majority of this FGM has a similar value of the freezing range to the pure IN718 alloy. This means the solidification condition and weldability of the whole FGM are semblable to the feature of pure IN718 alloy. As we know, IN718 has a good weldability, and the porosity is easy to escape from melt pool because of the long solidification time [85,86]. Therefore, there are no cracks and low porosity rate in the FGM though SS316 and IN718 have different CTEs [33, 71]. In addition, it exhibits that the porosity rate is tentatively increased when the composition approaches IN718. This is because of the nucleation of porosity influenced by the stability of melt pool, which is tied to the viscosity and entropy. The viscosity (η) at the temperature dependence can be expressed as the Arrhenius form [87-89]:

$$\eta = \eta_0 \, exp(E/RT) \qquad (1)$$

where η_0 is the pre-exponential viscosity and E is the activation energy for viscous flow, which are both constants for a particular element, T is the temperature in K and R is the gas constant. The viscosity data for Fe and Ni elements is listed in Table 2. Combining equation (1) and this data list, it can

 doi:10.20944/preprints202204.0139.v1

be deduced that the component with high Ni content has a lower viscosity, and vice versa. It indicates the melt pool with high weight percent of IN718 is unstable to collapse for entrapping pores when the laser beam irradiates into the melt pool. Furthermore, Fig. 2f provides the alloy entropy with different compositions. The excess entropy decreases gradually as the percent of IN718 increases, while it locates the composition range around 75wt.% has the highest nominal entropy, which gives more motion energy to cause the pedesis more severely in the liquid. It will further result in the unstable melt pool to collapse to entrap pores, leading to the increase in porosity. This computation on the physico-chemical properties of different compositions through the high-throughput thermodynamic modeling provides a high-throughput approach to understand and study the relationship between defects and composition, which is promising to not only predict the properties according to composition, but also perform composition design for new alloy development in the further.

Table 2. Data for viscosity of Fe and Ni elements [87-89]

Element	Melting point T_m (°C)	$\eta(T_m)$ (mPa·s)	η_0 (mPa·s)	E (kJ·mol^{-1})
Fe	1535	5.5	0.370	41.4
Ni	1455	4.9	0.166	50.2

3.1.2. Microstructure evolution along the composition gradient

Figure 4a shows the metallurgical morphologies of the as-deposited FGM changing from pure SS316 to pure IN718. It shows the structure with all compositions consist of numerous dendrites. As the weight percent of IN718 increases, the primary dendrites get shorten and the shape of dendrites transfer from columnar to cellular. It is attributed to the increased heat capacity and freezing range of the component with the weight percent of IN718 increasing, as elucidated in Fig. 2e. The cooling rate and anisotropy of solidification are consequently reduced, which is susceptible to form equiaxial grains and cellular dendrite networks. Observed on SEM, it can be seen that except the pure SS316, there are a lot of secondary phase segregated along the grain boundaries in the components. According to the Scheil simulation as exampled in Figs. 3a2 and 3b2, it is supposed to the nonequilibrium phase (i.e., Laves) in the as-deposited FGM. In the magnified images, they show irregular shape. Their size and clustering degree increase gradually. The EDS result embedded in the image of Fig. 4a indicates they are rich of Nb, which further confirms the Laves phase formation. Performing the high-throughput Scheil simulations via TC-Python approach, the phase fraction of Laves as a function of composition was generated to plot in Fig. 4b. The Scheil modeling was chosen because it is a nonequilibrium simulation, which has a similar status of laser deposition. From Fig. 4b, it is clear to see that the phase fractions of Laves predicted by TCFE9 and TCNI8 are significantly different, deviating from each other when the weight percent of IN718 is greater than 25wt.%. Whereas, they have the same trend, i.e., increasing first and keeping a relatively high value, and decreasing eventually. The experimental data of the Laves phase extracted from systematic SEM observations was also summarized in Fig. 4b. It

Preprints (www.preprints.org) | NOT PEER-REVIEWED | Posted: 15 April 2022 doi:10.20944/preprints202204.0139.v1

demonstrates the prediction of Laves phase by TCNI8 has a good agreement with the experimental result, which indicates TCNI database plays a better prediction for Ni-rich alloy (the composition is approximately higher than 20 wt.% Ni) rather than TCFE database.

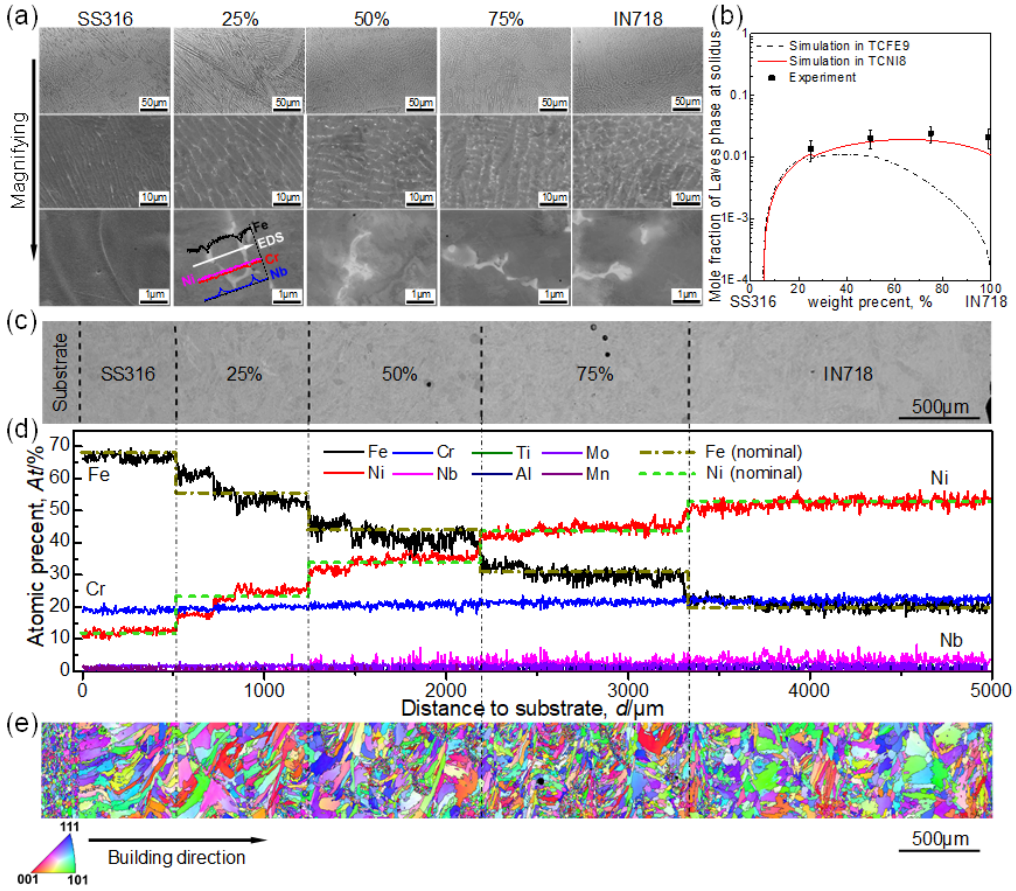

Figure 4. SEM analysis on the entire as-deposited FGM along building direction: (a) OM and SEM morphologies, (b) Laves phase fraction vs. composition of computational and experimental results, (c) overall BSE images of the whole FGM cross section, (d) overall EDS profiles and (e) IPF crystal orientation mapping.

Figures 4c-4e show the EDS and EBSD profiles via SEM over the whole FGM along building direction. The EDS analysis was conduct on the finely polished flat surface (Fig. 4c) of the as-deposited FGM without etching. It is obvious that the major elements of Ni and Cr have equal proportional increases, and Fe has an equal proportional decrease from pure SS316 to pure IN718 (Fig. 4d). The alloying element of Nb has a corresponding increase gradually. Other alloying elements cannot be quantified accurately due to their low values of contents. However, because the gradient compositions were mixed by two pure powders of SS316 and IN718 with certain weight ratios, all of the elements have the same ratio change in each mixed composition. The major elements of Fe and Ni can represent the real controlling accuracy for the whole gradient compositions. It can be illustrated that there is a flat composition profile in each component that changes from pure SS316 to pure IN718, except few small deviations between each layer, like in the compositions of 25wt.% and 50wt.%. Further comparing the

 doi:10.20944/preprints202204.0139.v1

measured composition to the nominal (designed) composition by two representative elements of Fe and Ni, it reveals a well agreement with each other, which demonstrates the successful build of this FGM with a decent control on composition.

The stitched overall EBSD mapping exhibits the grain evolution as the composition changes (Fig. 4e). Only one face center cubic (FCC) phase of the matrix exists in the whole FGM, because both SS316 and IN718 have FCC matrix, as also confirmed in Fig. 3. There are no sharp interfaces between the components with each composition (Fig. 4e). each interface has a small gradient zone, especially for those near the higher content of IN718, as demonstrated in EDS profiles of Fe and Ni in Fig. 4d. The gradient zone along each interface lowers the mismatch of printability for two individual compositions, which reduces the possibility of cracks. Another phenomenon worth to notice is that the grains grow from columnar shape to equiaxial form as the weight percent of IN718 increases. This is consistent with the OM observation in Fig. 4a, which further confirms the effect of heat capacity and freezing range on the solidification and grain growth.

3.2. Post-heat treatments on gradient smoothing and microstructure improvement

As we know, homogenization is not only an effective post heat-treatment method to eliminate the heterogeneity inherited from the AM process, but also a promising way to smooth the gradient on composition and microstructure for the FGM building and eventually obtain a good gradient property. Therefore, different post homogenization heat treatments were conducted to investigate the utility of post heat treatments on gradient smoothing and microstructure improvement.

3.2.1. Effect of homogenization on microstructure and composition

Figure 5 shows the microstructural and compositional evolution of the FGM samples homogenized at 1200°C for 1 h and 7 d (168 hours), respectively. From Figs. 5a and 5b, it exhibits that after 1 h homogenization, the heterogeneous structure with different columnar grains and strong textures has been removed, replacing with equiaxial grains. Grains grow significantly and Laves phase is completely removed. However, there are a lot of precipitates present in the FCC matrix, as seen in Fig. 5a. They are supposed to be the MX secondary phase, which is confirmed in the thermodynamic predictions at 1200°C (Figs. 3a1 and 3b1). M consists of the major elements of Nb and Ti, and X contains the elements of C and N for this FGM. Their volume fractions increase gradually as the weight percent of IN718 increases, which is attributed to be the increase in Nb content in different components. The MX precipitates increase with a bigger size after 7 d homogenization (Fig. 5d). The Laves phase is absent in the coarsened FCC matrix.

Preprints (www.preprints.org) | NOT PEER-REVIEWED | Posted: 15 April 2022 doi:10.20944/preprints202204.0139.v1

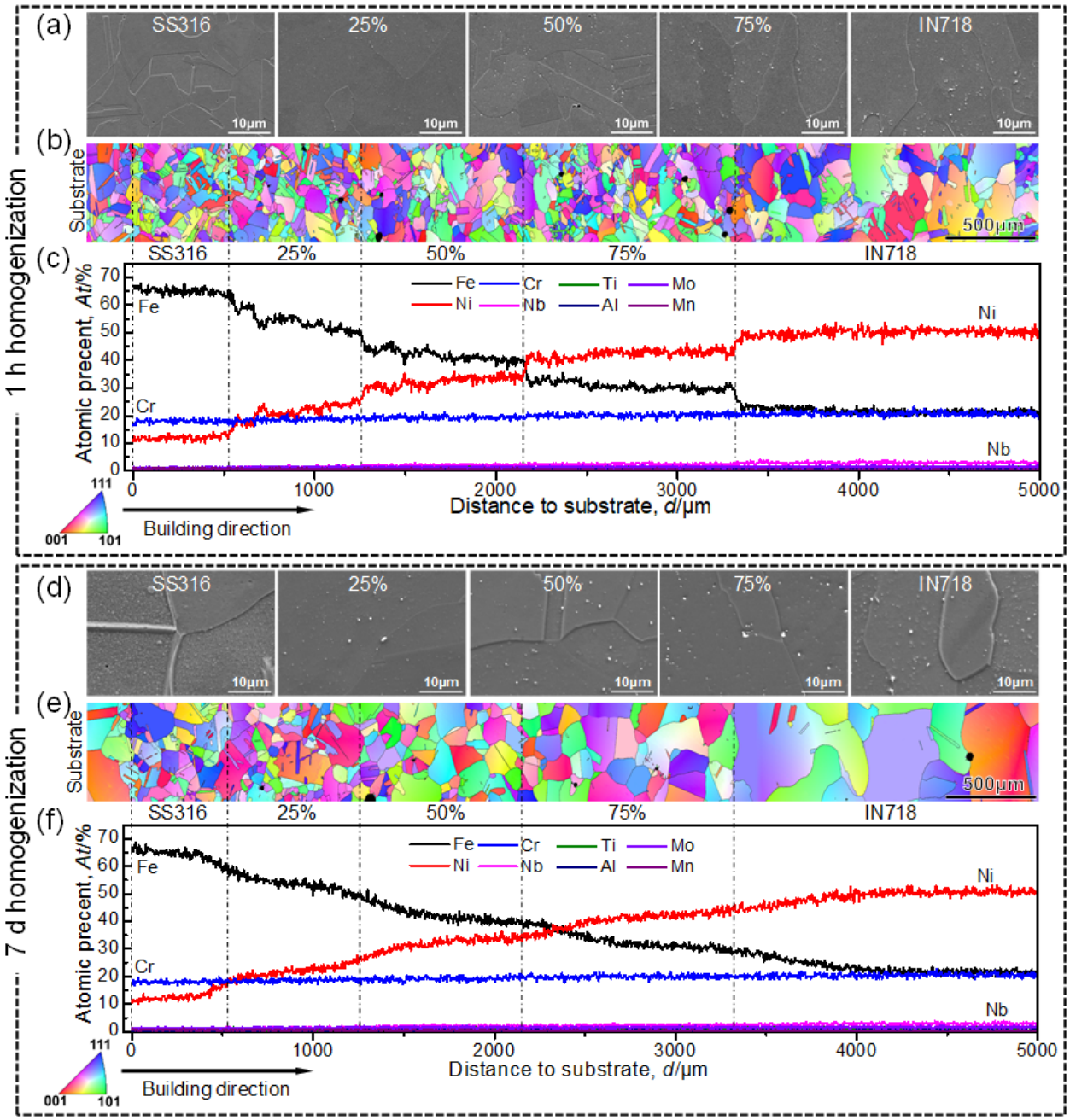

Figure 5. Electron microscopy analysis on the whole FGM along building direction after homogenization at 1200 °C: SEM morphologies (a), IPF crystal orientation mapping (b) and EDS profiles (c) with 1 h homogenization; SEM morphologies (d), IPF crystal orientation mapping (e) and EDS profiles (f) with 7 d homogenization.

The EBSD maps present a significant change on grains with the homogenization time increasing (Figs. 5b and 5e). The grains grow up and become much more homogenous in each compositional component after homogenization, compared with the as-deposited FGM. However, the grains of AM pure SS316 are always smaller than those in substrate which is traditionally wrought SS316L steel. This provides an evidence of the

Preprints (www.preprints.org) | NOT PEER-REVIEWED | Posted: 15 April 2022 doi:10.20944/preprints202204.0139.v1

advantageous response of AM alloys on post heat treatments compared with the traditional fabrication method. The overall grain evolution in the FGMs is summarized in Fig. 6 based on the EBSD results.

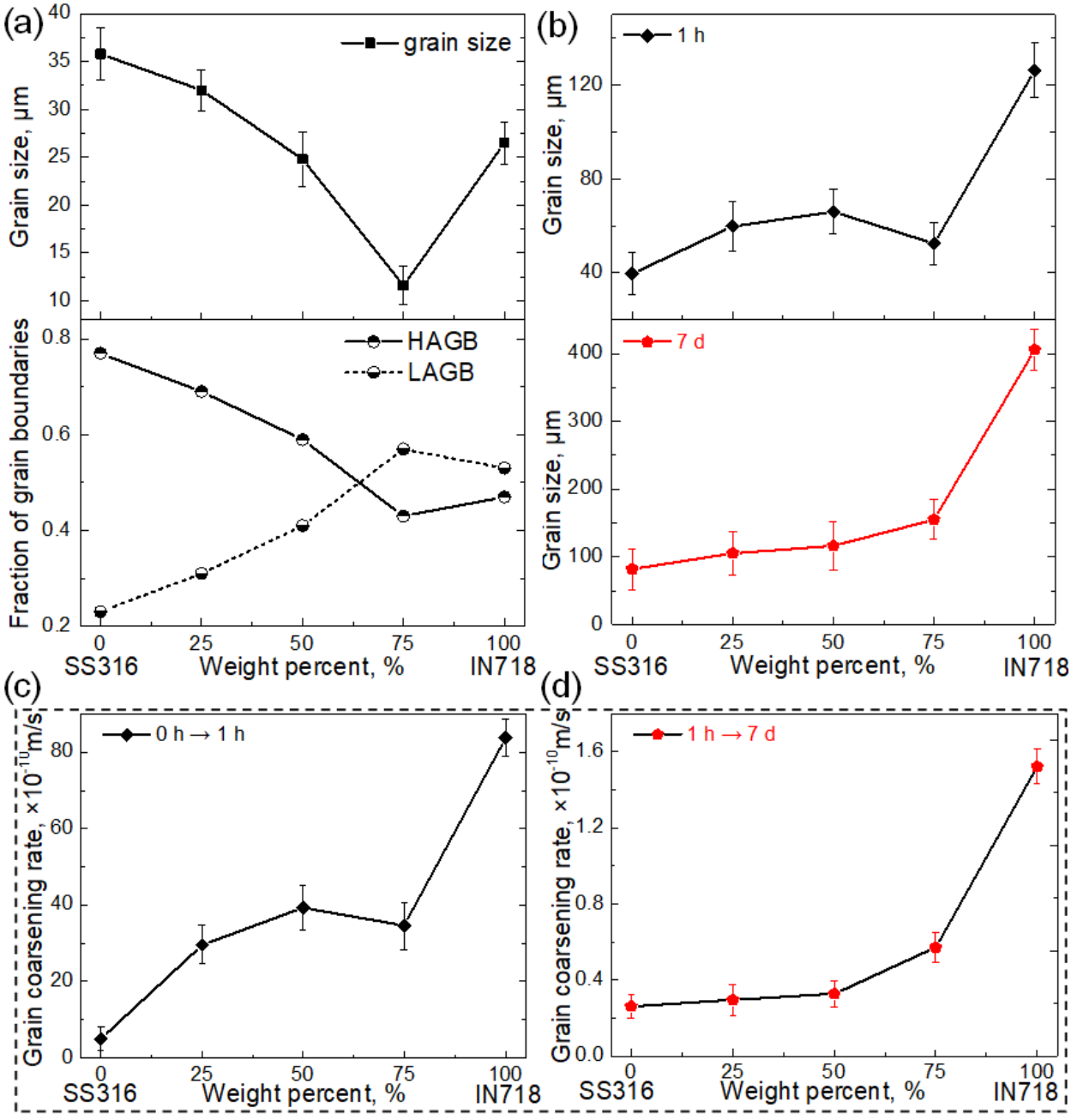

Figure 6. The grain evolution of EBSD analysis in the FGM with different compositional components after different homogenization heat treatments: (a) as-deposited condition (data extracted from Fig. 4e), (b) 1 h and 7 d homogenization at 1200 °C, respectively, (c) grain coarsening rate of different compositional components during 1 h homogenization (recrystallization) and (d) grain coarsening rate of different compositional components from 1 h to 7d homogenization (grain growth).

For the as-deposited FGM showed in Fig. 4e, the grain size decreases from 36 μm first and then increases up to 27 μm, as the weight percent of IN718 increases. The component with 75wt.% IN718 has the finest grain size

Preprints (www.preprints.org) | NOT PEER-REVIEWED | Posted: 15 April 2022 doi:10.20944/preprints202204.0139.v1

of 12 μm which is half of pure IN718 and one third of pure SS316 (Fig. 6a). The found of this critical composition on the grain size can be explained by the entropy of this component. As we know, high entropy alloys exhibit good thermal stability due to the high mixing alloy entropy that has resistance to the grain growth [90-92]. It is attributed to sluggish long-range substitutional diffusion because of the lack of a major diffusion element and the necessity of cooperative diffusion of constituent atoms in order to have proper composition partitioning [90,93]. Accordingly, 75wt.% IN718 component has the highest mixing alloy entropy in all these compositions changing from pure SS316 to pure IN718, as calculated in Fig. 2f. This results in the finest grain in the as-deposited component with the composition of 75wt.% IN718. Moreover, the fraction of grain boundaries of high angle grain boundary (HAGB) extracted from the EBSD data shows that it has the same trend as the grain size (downside of Fig. 6a). Consequently, the fraction of low angle grain boundary (LAGB) has a contrary evolution, with the highest value at 75wt.% IN718. The LAGB reflects the residual stress and distortion in the grains [94-97]. Hence, there is a big amount of distortion in the 75wt.% IN718 component. It is ascribed to the dislocations stemming from the laser deposition and precipitation of Laves phase in the solidification. Because of the finest grains, the restriction between different small grains triggers the increase of dislocations during the grain growth. In addition, the phase fraction of Laves precipitated in the 75wt.% IN718 component is highest, which contributes to the big distortion surrounding their interfaces with the matrix. Above all, this 75wt.% IN718 component with fine and equiaxial grains directly obtained from the laser deposition has a great potential for use in AM industry with the advantage of avoiding post heat treatments. It can be developed as a new alloy for AM, which will be further studied in the future work.

After 1 h homogenization at 1200°C, the grain in pure SS316 component grows up to 40 μm with the equiaxial size. The grain size increases as the weight percent of IN718 increases, while it has a drop for the component with 75wt.% IN718 with a size of 52 μm (upside of Fig. 6b). When the composition of IN718 is higher, the grain size increases rapidly to 125 μm in the pure IN718 component. In the contrast, the grains get coarsened seriously after 7 d homogenization, especially for the pure IN718, of which the grain size increases up to 406 μm (downside of Fig. 6b). Based on the kinetics theory of grain growth, the grain growth here can be expressed as follows [98-100],

$$R(t)^2 - R_0^2 = kt \quad (2)$$

where $R(t)$ is the average grain radius at time t, and R_0 is the initial grain radius at the time t_0. In this case, $R(t)$ for different compositional components is obtained from Fig. 6b and R_0 is correspondingly obtained from Fig. 6a, respectively. k is a constant which can be calculated using Equation (2). Thus the grain coarsening rates for different compositional components in the FGMs with 1 h homogenization, dR/dt (t=1 h) and 7 d homogenization, dR/dt (t=7-d) are evaluated, as shown in Fig. 6c, respectively. It reveals that pure IN718 has an extremely big grain coarsening rate during homogenization at 1200°C. However, the components with the composition below 75wt.% IN718 has a relatively slow grain coarsening.

 doi:10.20944/preprints202204.0139.v1

Especially for the composition around 75wt.% IN718, the component has a good thermal stability and resistance to grain coarsening, with a microstructural behavior far away from both of pure IN718 and pure SS316.

Nevertheless, the homogenization heat treatment also changes the composition profiles significantly, as presented by the EDS analysis across the whole FGMs in Figs. 5c and 5f. The elemental profiles of Fe, Ni and Cr are clear to be identified in the profiles, which represents the gradient change of the whole elements, as stated in Fig. 4d. The EDS profiles of homogenized FGMs become more and more smooth with reduced deviations as the homogenization time increases, which indicates the composition is more and more homogenous in the homogenized components. Compared with the EDS profiles of the as-deposited FGM (Fig. 4d), the interface zone with the gradient composition between each component increases after 1 h homogenization, and the composition profile in each composition forms a slope, not as flat as that in the as-deposited FGM. After the long term of homogenization for 7 d, the composition in the whole FGM has a continuous change with a very smooth gradient (Fig. 5f). The interfaces are bare to recognize in the EDS profile, which is also reflected in the EBSD results (Figs. 5b and 5e). These phenomena demonstrate the homogenization heat treatment has a significant effectiveness on the gradient smoothening of the composition and microstructure in the FGMs. The intrinsic reason is ascribed to the sufficient diffusion of elements at the high temperature of homogenization.

3.2.2. Kinetic modeling of diffusion behaviors in homogenization

To disclose the diffusion behaviors in this FGM in detail, the kinetic simulation at 1200°C was performed using the DICTRA modeling. Only FCC phase was included as the matrix, considering the absence of the Laves phase and liquidation at 1200°C. The simulation result is shown in Fig. 7a. It exhibits the simulated composition profiles of the major elements of Fe and Ni with the homogenization times of 0-h, 1-h, 24-h, 7-d and 21-d. The composition profile with 0 h homogenization means the nominal composition in the real distance of the FGM build. This profile was used as the input data to simplify the simulation, because the experimental result in the as-deposited FGM has a good agreement with the nominal composition (Fig. 4d). From Fig. 7a, it is clear to see that the compositional gradient becomes smoother as the simulated homogenization time increases. The elements diffuse fast between each component. Simultaneously, the diffusion interface has an obvious migration during homogenization, which moves to the Ni-rich side of alloys. This is because Ni has a faster diffusion rate than Fe in the Fe-Ni mutual diffusion system, which can be demonstrated by the diffusion coefficient of Fe and Ni as a function of composition via thermodynamic modeling in Fig. 7b. The simulated composition profiles of Fe and Ni after homogenization for 1 h and 7 d are extracted out to compare with the experimental EDS results, which are shown in Figs. 7c and 7d, respectively. They reveal good consistency with the experimental results, which demonstrates that the detailed diffusion behaviors in this FGM as a function of homogenization time can be well predicted using this kinetic modeling to further help the experimental designs. Nonetheless, the experimental results show a smoother compositional gradient without obvious plateaus. It indicates the

Preprints (www.preprints.org) | NOT PEER-REVIEWED | Posted: 15 April 2022 doi:10.20944/preprints202204.0139.v1

actual elemental diffusion is faster than the simulations. This is attributed to the faster diffusion of elements in the intergranular mode than that in the transgranular mode [101-103], while the DICTRA simulation considers only the transgranular diffusion to brief the modeling.

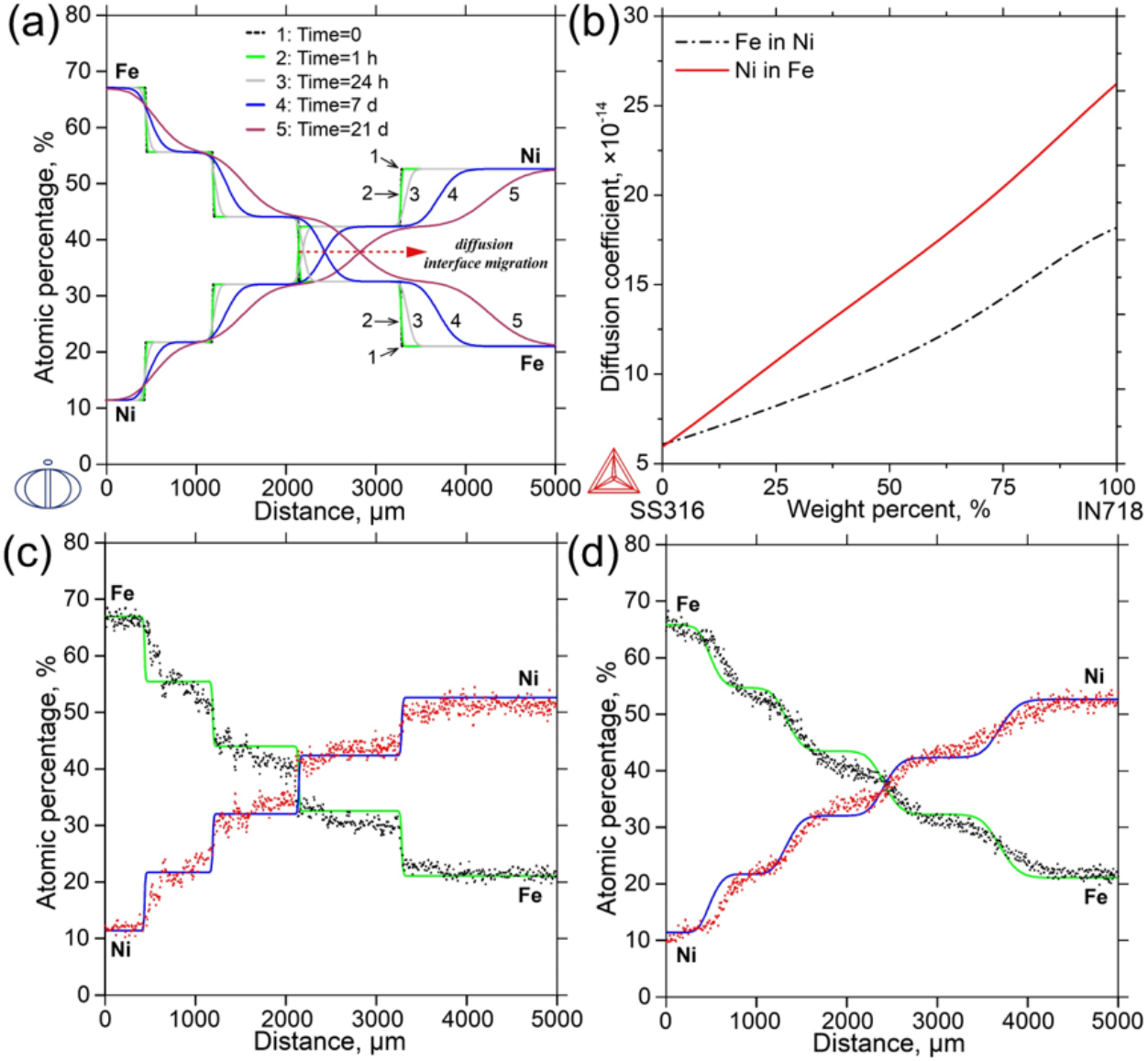

Figure 7. The kinetic simulation of diffusion using DICTRA modeling at 1200°C: (a) the simulated composition profiles of Fe and Ni elements with different homogenization times, (b) the calculated diffusion coefficients of Fe and Ni in Fe-Ni mutual diffusion system vs. composition of the FGM using thermodynamic modeling, (c) comparison of the composition profiles of Fe and Ni elements between experimental EDS results and simulation results after 1 h homogenization and (d) comparison of the composition profiles of Fe and Ni elements between experimental EDS results and simulation results after 7 d homogenization.

3.3. Aging precipitation in FGMs: Experimental characterization and thermodynamic simulation

3.3.1. Precipitation behaviors in the as-deposited FGMs.

Because the synergistic effect of gradient compositions and nonequilibrium status from laser deposition, the precipitation behaviors

Preprints (www.preprints.org) | NOT PEER-REVIEWED | Posted: 15 April 2022 doi:10.20944/preprints202204.0139.v1

presented in FGMs during aging would have a significant difference from those in the alloys fabricated by the traditional methods. After aged at 718°C for 15 h, i.e., a peak aging status for IN718 alloy [104,105], the SEM morphologies of the microstructure in the components with different compositions were observed, respectively, as shown in Fig. 8. It shows that the Laves phase still remains in the matrix, even occurring in the matrix of pure SS316 after the long aging time (Fig. 8a). Compared with the as-deposited FGM, the volume fraction of Laves phase increases after aging. The segregation along columnar dendrites and cellular dendrites become more serious because of the increased precipitation. Nonetheless, there are new precipitates occurring around the Laves phase, as seen at the high magnification (Figs. 8a3-8e3).

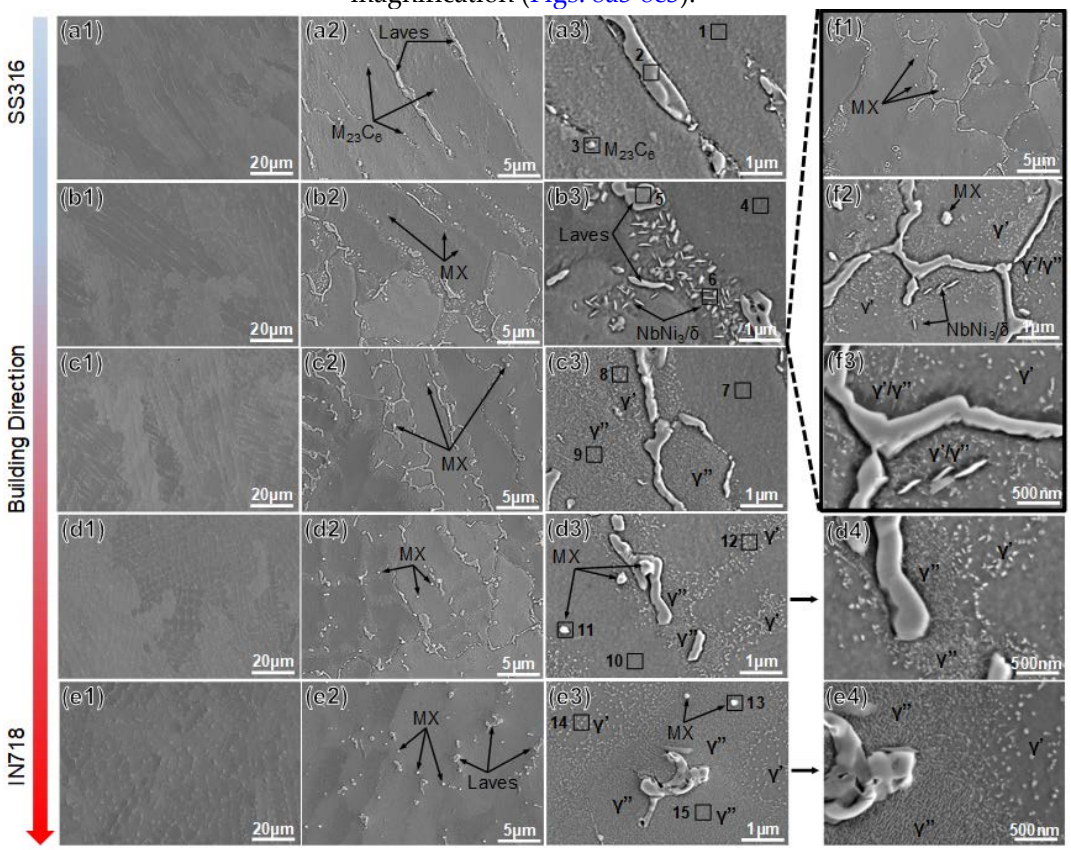

Figure 8. SEM morphologies of the microstructure in different compositional components of the aged FGM at 718 °C for 15 h: (a) Pure SS316, (b) 25wt.% IN718, (c) 50wt.% IN718, (d) 75wt.% IN718, (e) 100wt.% IN718 and (f) the interface zone between (b) and (c). ("1-4" present the images at different magnifications, the observed location is in the center zone of each component).

To clarify the precipitates in the aged FGM, the thermodynamic simulations via CALPHAD databases were performed to predict the phase fraction as a function of temperature for different compositions. Because aging for 15 h is a relative equilibrium status which is different from the as-deposited condition, the equilibrium CALPHAD databases were used for these simulations. Figure 9 shows the simulation results from TCFE9 and TCNI8 of pure SS316, 25wt.%, 75wt.% and pure IN718 components, respectively. The simulation result of 50wt.% IN718 has already been

Preprints (www.preprints.org) | NOT PEER-REVIEWED | Posted: 15 April 2022 doi:10.20944/preprints202204.0139.v1

provided in Figs. 3a1 and 3b1. Parallelly, several points on different phases were analyzed using electron probe microanalyzer (EPMA). which is listed in Table 3. In the pure SS316 component, there are plenty of irregular phases along the grain boundaries and many circular particles in the matrix (Fig. 8a2), which were analyzed as point 2 and point 3, respectively (Fig. 8a3). Point 1 of the matrix was tested for comparison. According to the tested composition, point 2 is rich of Fe, Cr and Mo. Point 3 is only rich of Cr and Mo and lack of Fe (Table 3). Based on the simulation (Fig. 9a1), the chemical formula of Laves phase is $(FeCr)_2Mo$ and the chemical formula of $M_{23}C_6$ is approximate $(CrMo)_{23}C_6$. Therefore, Laves phase (point 2) and $M_{23}C_6$ (point 3) are confirmed to form in pure SS316 during aging, combining the analysis of EPMA and thermodynamic simulation. Whereas, σ phase is not found during this aging. This may be ascribed to the poverty of Cr in the matrix because of the formation of Laves and $M_{23}C_6$ phases. Besides, the Laves phase is not rightly predicted in the TCNI8 simulation (Fig. 9a2).

Table 3. The EMPA result of different points in the components with different compositions (at.%)

Sample	Point	Ni	Fe	Cr	Nb	Ti	Al	Mo	Mn	Others	Supposed phase
0wt.%	1	11.91	67.5	18.4	0	0	0	1.12	1.05	Bal.	Matrix
	2	6.92	69.1	20.75	0	0	0	2.18	1.04	Bal.	Laves
	3	11.61	62.93	22.54	0	0	0	1.92	0.98	Bal.	$M_{23}C_6$
25wt.%	4	22.29	54.62	19.32	0.96	0.29	0.23	1.42	0.78	Bal.	Matrix
	5	23.43	38.94	15.17	12.64	1.64	0.17	7.2	0.73	Bal.	Laves
	6	26.41	50.01	18.06	2.62	0.28	0.27	1.48	0.76	Bal.	δ/$NbNi_3$
50wt.%	7	32.84	41.86	20.33	1.75	0.56	0.43	1.53	0.52	Bal.	Matrix
	8	36.83	32.99	19.09	1.93	3.25	3.62	1.58	0.48	Bal.	γ'/Ni_3Ti
	9	49.26	21.29	19.85	6.31	0.64	0.49	1.47	0.46	Bal.	γ''
75wt.%	10	42.01	31.42	20.46	2.34	0.83	0.69	1.7	0.28	Bal.	Matrix
	11	40.06	29.68	19.62	5.89	1.75	0.75	1.52	0.4	Bal.	MX
	12	45.28	20.7	19.72	2.53	4.82	4.7	1.66	0.27	Bal.	γ'/Ni_3Ti
100wt.%	13	50.04	17.12	20.51	6.12	2.1	1.87	1.8	0.03	Bal.	MX
	14	58.28	4.65	19.39	3.08	6.19	6.24	1.76	0.02	Bal.	γ'/Ni_3Ti
	15	66.16	3.45	18.23	8.13	1.15	0.86	1.6	0.02	Bal.	γ''

Preprints (www.preprints.org) | NOT PEER-REVIEWED | Posted: 15 April 2022 doi:10.20944/preprints202204.0139.v1

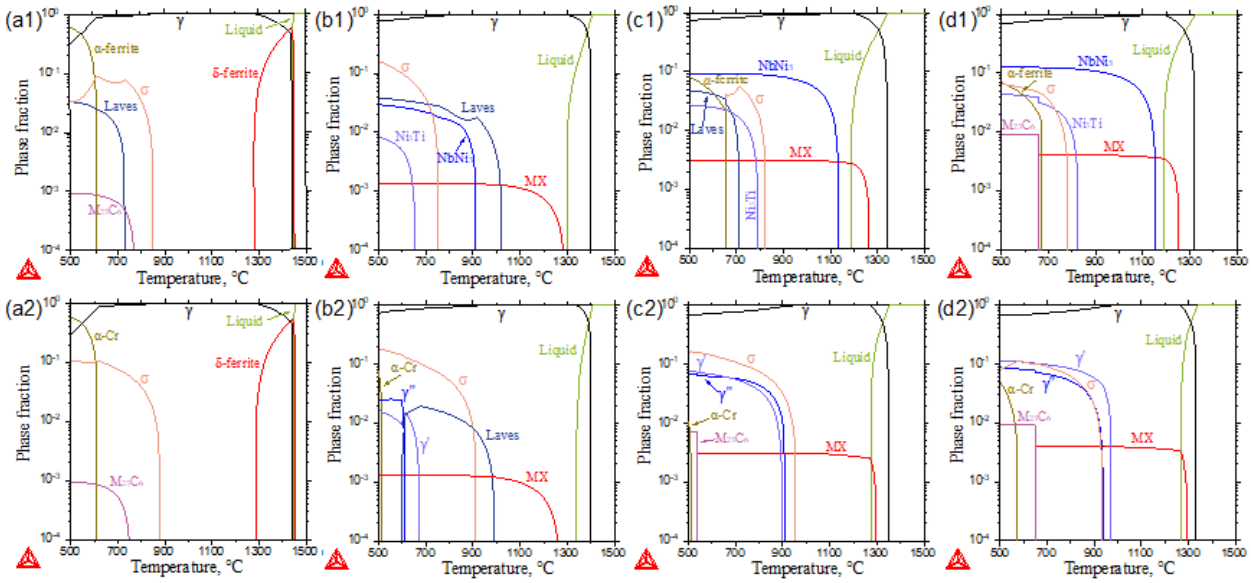

Figure 9. Thermodynamic predictions on phase fraction vs. temperature for different compositional components using TCFE9 and TCNI8 databases, respectively: (a) pure SS 316, (b) 25wt.% In 718, (c) 75wt.% In 718 and (d) 100wt.% In 718. (1-TCFE9 database, 2-TCNI8 database. The simulation results for 50wt.% In 718 is shown in Figs. 3a1 and 3b1) .

In the 25wt.% IN718 component, Laves phase still forms along the grain boundaries, with an increase volume (Figs. 8b). While the composition of this Laves phase is different, which is enriched with Nb, Ti and Mo instead of Fe and Cr elements (point 5 in Table 3). This fact is consistent with the simulation result (Fig. 9b). It is ascribed to the addition of alloying elements of Nb and Ti coming from the IN718 powder. Meanwhile, there are numerous needle-like secondary phase near the Laves phase, occupying the grain boundaries (Fig. 8b3). They have an enrichment of Ni and Nb (point 6), which are the chemical constituents of $NbNi_3$ predicted by Fig. 9b1. This phase of $NbNi_3$ is defined as δ phase in the TCNI8 database. Because δ phase is the stable phase and γ'' is the metastable phase in Ni-based superalloy, the δ phase is usually suspended in TCNI simulations to guarantee the formation of γ'' phase. That's why δ phase does not show in Fig. 9b2, replaced by γ' and γ'' phase. However, δ phase is commonly formed instead of γ' and γ'' phases, until the alloying elements like Nb, Ti reach a certain content in the Ni-based superalloys. Hence, the TCFE database has a good prediction for the component with low content of IN718. When the weight percent of IN718 increases to 50wt.%, δ phase is not found in the microstructure. Tremendous ultra-fine nanoprecipitates occur in the matrix, which is supposed to be γ' and γ'' phases. To confirm their formation, the EMPA (points 7-9) and thermodynamic simulation (Figs. 3a1 and 3b1) were combined to perform. According to the simulation result, γ' and γ'' phases are formed replacing of δ phase, with chemical formulas of $Ni_3(Ti, Al)$ and Ni_3Nb, respectively. Table 3 shows that point 8 (γ') is rich of Ni, Ti and Al. On the contrary, point 9 (γ'') is only rich of Ni and Nb. This is consistent with the prediction of thermodynamic simulation in TCNI8 (Fig. 3b1). It identifies that the finer nanoprecipitates surrounding the Lave phase are γ'' phase and the relatively bigger ones away from the Laves phase are γ' phase, which is also

Preprints (www.preprints.org) | NOT PEER-REVIEWED | Posted: 15 April 2022 doi:10.20944/preprints202204.0139.v1

demonstrated in the following analyses for 75wt.% and 100wt.% IN718 components (Figs. 8d4 and 8e4). The TEM analysis of γ′ and γ′′ phases in IN718 were studied in our previous work [106-108]. As the increased content of IN718, γ′ phase becomes richer of Ti and Al and γ′′ phase is enriched of more Nb (points 12, 14 and 15). They become separate from each other. The fraction of γ′′ phase increases, which is also well predicted in the simulations using TCNI8 database, as shown in Figs. 9c2 and 9d2. TCFE9 is not capable to the prediction for the components with much higher content of 25wt.% IN718. Whereas, the Laves phase remains in the prediction from TCFE9 database until 75wt.% IN718, which is consistent with the experimental result. However, since Laves phase is a metastable phase, it is difficult to get a good prediction from thermodynamic simulation using the AM components with directly aging. Beside the analyzed phases above, MX secondary phase is always formed in the matrix as long as the matrix has the alloying elements, which has been confirmed in the SEM observations (Figs. 8a2-8e2) and simulation results (Figs. 9b-9d). The enrichment of Nb, Ti and Al in the MX phase increases with the weight percent of IN718 increasing (points 11 and 13).

As elucidated above, the gradient components with different compositions have remarkably different precipitation behaviors and transformations between each phase. This kind of precipitation transformations can be found in the gradient interface between 25wt.% and 50wt.% IN718, as presented in Fig. 8f. $NbNi_3$ or δ phase is reduced and partially transformed to γ′/γ′′. Another intriguing precipitation behavior is that the formation of γ′′ is always near the Laves phase, and the formation of γ′ is far away from the Laves phase. Nonetheless, they are all nucleated and precipitated at grain boundaries. This is because the alloying elements like Nb, Ti and Al at grain boundaries is high due to the segregation, which is suitable to form alloying element-rich γ′ and γ′′ phases. Furthermore, during the isothermal aging heat treatment, the Laves phase gets dissolved gradually and releases the alloying elements, especially the element of Nb. Therefore, the Nb-rich γ′′ phase is easy to form in the Nb-enriched area near the Laves phase. The Ti-rich γ′ phase is formed far away from the Laves phase because of the poverty of Nb. These nucleation and transformation between different phases are important and worth to exploit for the development of new FGMs using AM.

3.3.2. Precipitation behaviors in the homogenized FGMs.

The aging heat treatment at 718°C for 15 h was carried out based on the homogenized samples of the FGM build. Figure 10 presents the microstructural evolution in different compositional components with different homogenization times via HRSEM observations. The area observed on the SEM was taken from the center location of each component. For the 1 h homogenized FGM followed by aging, the microstructure consists of big austenite grains and numerous precipitation phases (Figs. 10a-10e). The precipitates are similar to those in the as-deposited FGM after aging, as predicted in the thermodynamic simulations (Fig. 9). However, the morphologies and volume fractions of these precipitates are of big differences. Compared with the microstructure of the 1 h homogenized FGM, after aging, the Laves phase occurs with a small amount along the grain

Preprints (www.preprints.org) | NOT PEER-REVIEWED | Posted: 15 April 2022 doi:10.20944/preprints202204.0139.v1

boundaries in the components those have a composition from 0wt.% to 50wt.% IN718, while it is absent in the components with 75wt.% and 100wt.% IN718. There is no σ phase present in the matrix. The volume fraction of MX precipitates increases as a function of composition. Meanwhile, MX precipitate becomes much bigger than that in the as-deposited FGM, with the cubic or polygonal shapes (Figs. 10c-10e). δ or $NbNi_3$ phase occurs in the component with 50wt.% IN718. They are precipitated along sub-grain boundaries, as showed in Fig. 10c. When the composition increases to 75wt.% IN718, there are only MX, γ′ and γ′′ phases in the components (Figs. 10d and 10e). It is well known that the γ′ phase usually shows a cubic shape while the γ′′ phase forms with a needle-like shape [72,75,105]. As it can be seen, the γ′ and γ′′ phases are mixed with each other with very high density in these components, which is significantly different from the as-deposited FGM after aging. The absence of the Laves phase contributes the high density of the γ′ and γ′′ precipitates. Their fraction and size increase with the weight percent of IN718 increasing. It also indicates that the high content of Nb is suitable to form the γ′′ phase rather than the δ phase no matter the FGM structure is homogenized or not. This is consistent with the computational results in TCNI8 simulations rather than those in TCFE9 simulations (Fig. 9).

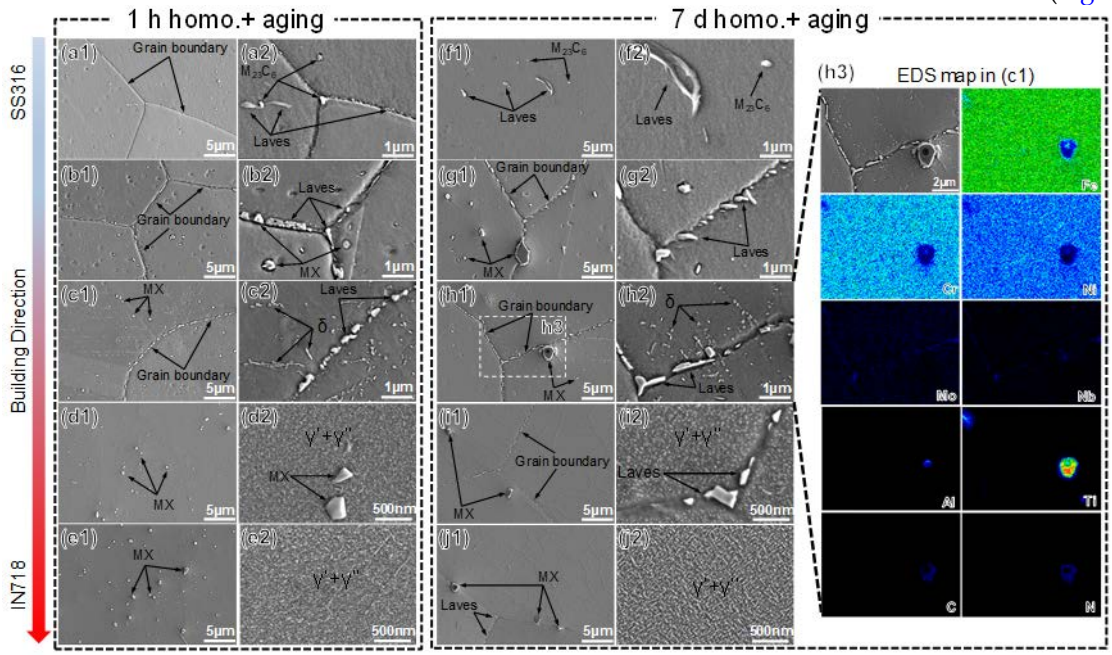

Figure 10. SEM morphologies of the microstructure in different compositional components with 1 h (a-e) and 7 d (f-j) homogenization at 1200 °C followed by aging at 718 °C for 15 h: (a) and (f) Pure SS316, (b) and (g) 25wt.% IN718, (c) and (h) 50wt.% IN718, (d) and (i) 75wt.% IN718, (e) and (j) 100wt.% IN718, (h3) EDS mapping of the area in (h1). ("1-3" present the images at different magnifications, the observed location is in the center zone of each component).

After the long term of homogenization for 7 d, the aging precipitation behaviors is also different from those in the 1 h homogenized FGM (Figs. 10f-10j). The Laves phase appears back in all the components after aging. This is supposed to be that the long term of homogenization makes the elements very uniform in the matrix and grain boundaries. During aging, the γ′ and γ′′ phases prefer to form in the matrix rather than in the grain boundaries

 doi:10.20944/preprints202204.0139.v1

[104,105]. It provides the high driving force of uphill diffusion of the elements from the grain boundaries to the matrix to form γ′ and γ′′ phases [109,110]. However, the diffusion velocity of Ni is much faster than Nb and Mo. It leads to the poverty of Ni and the segregation of Nb and Mo in the grain boundaries, which is suitable to the formation of the Laves phase. Except this difference from the 1 h homogenized FGM after aging, the precipitation behaviors of the other phases are similar in the 7 d homogenized FGM. Whereas, the size of the MX, γ′ and γ′′ phases increase obviously (Figs. 10g1 and 10j1), especially for the MX precipitates. Meanwhile, the elemental constitution of MX is different, showing a darker contrast under the SEM observation compared with that in the as-deposited and 1 h homogenized FGMs. Figure 10h3 presents the EDS mapping of the area in the component with 50wt.% IN718. It can be seen that the MX has much more enrichment of Al and Ti than that of Nb. The dark area in the MX represents the enrichment of Al, which gives a dark contrast because of the light element. In addition, the MX is highly enriched with N. Hence, the MX in the long term of homogenization has more content of Al and Ti and less content of Nb. This is possibly because the high density of the formation of Nb-rich γ′′ phase results in the poverty of Nb in the MX precipitates. Besides, the enrichment of Mo and Nb in the grain boundaries demonstrates the presence of the Laves phase. From the above, it is well elucidated that the homogenization has a remarkable effect on the following aging precipitation behaviors in the FGMs. The big difference of homogenization and aging effects can lead to the corresponding response of mechanical properties, which will be discussed in Section 3.4.

3.3.3. Uncertainty evaluation of thermodynamic modeling via the hybrid high-throughput design on experiment and computation

In this work, the FGM with the gradient composition and microstructure was built using the DED additive manufacturing technology combined with the post heat treatments. Meanwhile, the high-throughput thermodynamic modeling was performed using the CALPHAD-based TC-Python method to study phase evolution with a continuous change of the composition, providing a prediction to in turn guide the experimental design and characterization. As elucidated above, the high-throughput computation of equilibrium modeling and Scheil-Gulliver modeling has been conducted to prediction the phases in the FGM (Figs. 3, 4b and 9). However, the quality of CALPHAD-based thermodynamic modeling is significantly limited not only by the available thermo-chemical and phase stability data but also by the intrinsic uncertainty of the model structure [111]. Since nowadays the thermodynamic modeling relies more and more on the first-principle calculations to estimate the thermodynamic properties of phases, and the phase states observed in the experiments is difficult to guarantee to truly correspond to the theoretical thermodynamic equilibrium states, the discrepancies between calculations and experiments attract more and more attention to address their uncertainty [111-113]. To evaluate the uncertainty of the high-throughput thermodynamic modeling performed in this work, three thermodynamic conditions of the FGMs with different compositions were designed to provide different experimental phase states, i.e., as-deposited+aging, 1 h homo.+aging and 7d homo.+aging, to compare with the

Preprints (www.preprints.org) | NOT PEER-REVIEWED | Posted: 15 April 2022 doi:10.20944/preprints202204.0139.v1

theoretical equilibrium states used in the thermodynamic modeling. Furthermore, two thermodynamic databases, i.e., TCFE9 and TCNI8 databases were used for the high-throughput modeling on the FGMs from Fe-based alloy to Ni-based alloy.

The equilibrium phase fractions as a function of weight percent of IN718 at the temperature of 718°C was calculated using TC-Python high-throughput thermodynamic modeling, as showed in Fig. 11. Meanwhile, the phase fractions in five different compositional components in the FGMs with three thermodynamic conditions were statistically extracted from the high-resolution SEM observations. Each data was combined on several SEM images and repeatable, which is incorporated in Fig. 11. The lines in the figure present simulation results, and the points present experimental results. Figure 11a exhibits that at the aging temperature of 718°C, it has the same trend on the prediction of the austenite matrix, MX, σ and Laves phases by TCFE9 and TCNI8 simulations. The fraction of MX increases as the weight percent of IN718 increases. Whereas, the detailed evolution of σ and Laves phases as a function of composition is different, especially for the Laves phase. In the TCFE9 prediction, the Laves phase occurs at the beginning composition (pure SS316) and keep its presence until the composition reaches ~75wt.% IN718, while it only begins to occur at ~5wt.% IN718 and ends at ~45wt.% IN718 in the TCNI8 prediction. Both of them have a big difference from the experimental result, of which the Laves phase is always present in all gradient compositions of the "as-deposited+aging" FGM. This is possibly because the direct aging heat treatment for 15 h without homogenization is not enough to get the equilibrium condition of the metastable Laves phase. Besides, for the Ni-rich phases like $NbNi_3$, Ni_3Ti, γ′ and γ″, they have different predictions in TCFE9 and TCNI8 simulations. Thereinto, Ni_3Ti in TCFE database is named as γ′ in TCNI database. $NbNi_3$ in TCFE database is named as δ in TCNI database, which was suspended in TCNI simulation to make the occurrence of γ′ and γ″ (Fig. 11a2). Comparing these two simulations, it is easy to see that the predictions on γ′ and γ″ phases in TCNI8 simulation have much better agreement with the experimental results than those on $NbNi_3$ and Ni_3Ti phases in TCFE9 simulation. This indicates that TCNI database has a good prediction for Ni-rich phases.

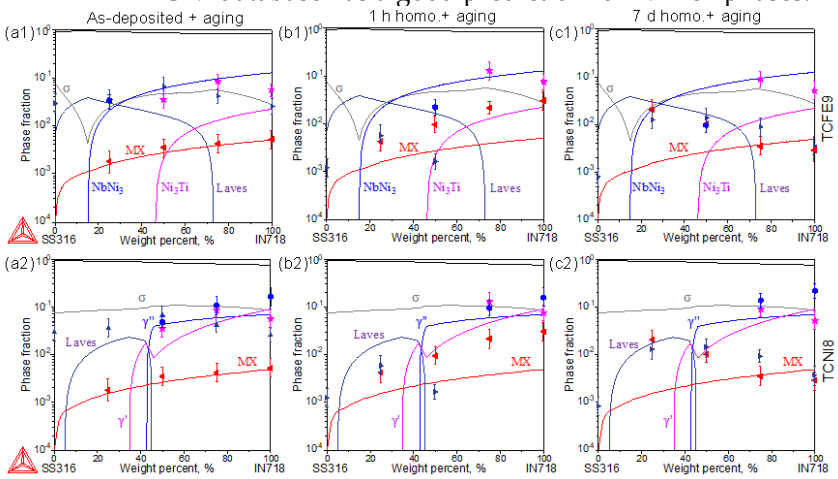

Fig. 11. Phase fraction vs. composition in the FGM from TC-Python high throughput thermodynamic modeling and experiments with aging heat treatment at 718 °C for 15 h: (a)

 doi:10.20944/preprints202204.0139.v1

as-deposited+aging thermodynamic state, (b) 1 h homo.+aging thermodynamic state and (c)7 d homo.+aging thermodynamic state. (1-TCFE9 database, 2-TCNI8 database. lines represent simulation results, points represent experimental results).

Preprints (www.preprints.org) | NOT PEER-REVIEWED | Posted: 15 April 2022 doi:10.20944/preprints202204.0139.v1

Similarly to the analysis for the "as-deposited+aging" FGM, the phase fractions of five different compositional components in the FGMs with the "1 h homo.+aging" and "7d homo.+aging" conditions are shown in Figs. 11b and 11c. From the figures, it can be seen that the phase fractions and their discrepancies between the thermodynamic simulations and experiments on the phases are very different under different thermodynamic experimental conditions and modeling databases.

To further evaluate the uncertainty of thermodynamic modeling on the prediction of phases, the prediction accuracy of phases is defined as below:

$$A_P = 1 - |f_i^s - f_i^e| / f_i^x \quad (2)$$

where f_i^s is the fraction of i phase from the simulation and f_i^e is the fraction of i phase from the experiment result. f_i^x depends on x, i.e., $x = s$ if $f_i^s > f_i^e$, $x = e$ if $f_i^s < f_i^e$. The A_P value of different phases is summarized in Table 4. The A_P value of each phase is an average of A_P values of each phase in all five compositional components. The detailed volume fraction of each phase from simulations and experiment results in each component is listed in Table 5. As the σ phase does not appear in the FGM and $M_{23}C_6$ only occurs in the pure SS316 component, the A_P analyses on σ and $M_{23}C_6$ phases are not included. The corresponding changes of A_P values under different simulation databases and thermodynamic conditions are illustrated in Fig. 12. For the as-deposited+aging condition, all databases have good predictions on the MX phase (Figs. 12a and 12b). Furthermore, TCNI8 has high prediction accuracies for the MX, δ, γ′ and γ′′ phases, except the Laves phase (Fig. 12b). The reason is supposed to be that the metastable Laves phase is not in the equilibrium state due to the direct aging heat treatment for 15 h without homogenization. The prediction on the Laves phase using these two databases under 1 h homo.+aging condition has the highest accuracy among these three thermodynamic conditions. Whereas, comparing all thermodynamic conditions, TCNI8 database has a relatively high prediction accuracies on phases than TCFE9 database. As further presented in Fig. 12c, the average prediction accuracy on all phases using TCNI8 database is always higher than that using TCFE9 database for all three thermodynamic conditions. In summary, the uncertainty of thermodynamic modeling is evaluated through the hybrid high-throughput design on experimental conditions and computational databases, which is significantly valuable to realize the vision on the quantitative prediction of precipitation behaviors. TCNI database is capable for prediction on the Ni containing alloys. The short term of homogenization like 1 h followed by aging is suitable for the experimental method to assess the thermodynamic databases of precipitation.

Table 4. The prediction accuracy (A_p) of different phases

Phase	As deposited+aging		1 h homo.+aging		7 d homo.+aging	
	TCFE9	TCNI8	TCFE9	TCNI8	TCFE9	TCNI8
Laves	0.266	0.098	0.492	0.465	0.276	0.145
MX	0.901	0.876	0.401	0.393	0.571	0.576
δ	0.32	0.8	0.275	0.6	0.233	0.6
γ'	0.519	0.67	0.478	0.641	0.514	0.618
γ"	0	0.766	0	0.611	0	0.549
Average	0.401	0.642	0.329	0.542	0.319	0.498

Preprints (www.preprints.org) | NOT PEER-REVIEWED | Posted: 15 April 2022 doi:10.20944/preprints202204.0139.v1

Table 5. The volume fractions of phases in different components.

Phase	Compositional component, wt.% IN718	Simulation		Experiment		
		TCFE9	TCNI8	As deposited +aging	1 h homo. +aging	7 d homo. +aging
Laves	0	0.007	0	0.0294	0.0012	0
	25	0.0297	0.0173	0.0352	0.0056	0.0125
	50	0.0163	0	0.0662	0.0016	0.0138
	75	0	0	0.0416	0	0.0089
	100	0	0	0.0254	0	0.0036
MX	0	0	0	0	0	0
	25	0.0016	0.0015	0.0018	0.0042	0.0206
	50	0.0027	0.0026	0.0035	0.0095	0.0102
	75	0.0038	0.0037	0.0042	0.0213	0.0035
	100	0.0049	0.0048	0.0052	0.0302	0.0029
δ/$NbNi_3$	0	0	0	0	0	0
	25	0.0201	0	0.0336	0	0
	50	0.0587	0	0	0.022	0.0096
	75	0.0926	0	0	0	0
	100	0.1241	0	0	0	0
γ'/Ni_3Ti	0	0	0	0	0	0
	25	0	0	0	0	0
	50	0.0021	0.0129	0.0349	0	0
	75	0.0126	0.0465	0.0835	0.127	0.0892
	100	0.0219	0.0896	0.0568	0.075	0.0511
γ"	0	0	0	0	0	0
	25	0	0	0	0	0
	50	0	0.0417	0.0482	0	0
	75	0	0.0583	0.1075	0.095	0.136
	100	0	0.0689	0.1634	0.1564	0.2162

Preprints (www.preprints.org) | NOT PEER-REVIEWED | Posted: 15 April 2022 doi:10.20944/preprints202204.0139.v1

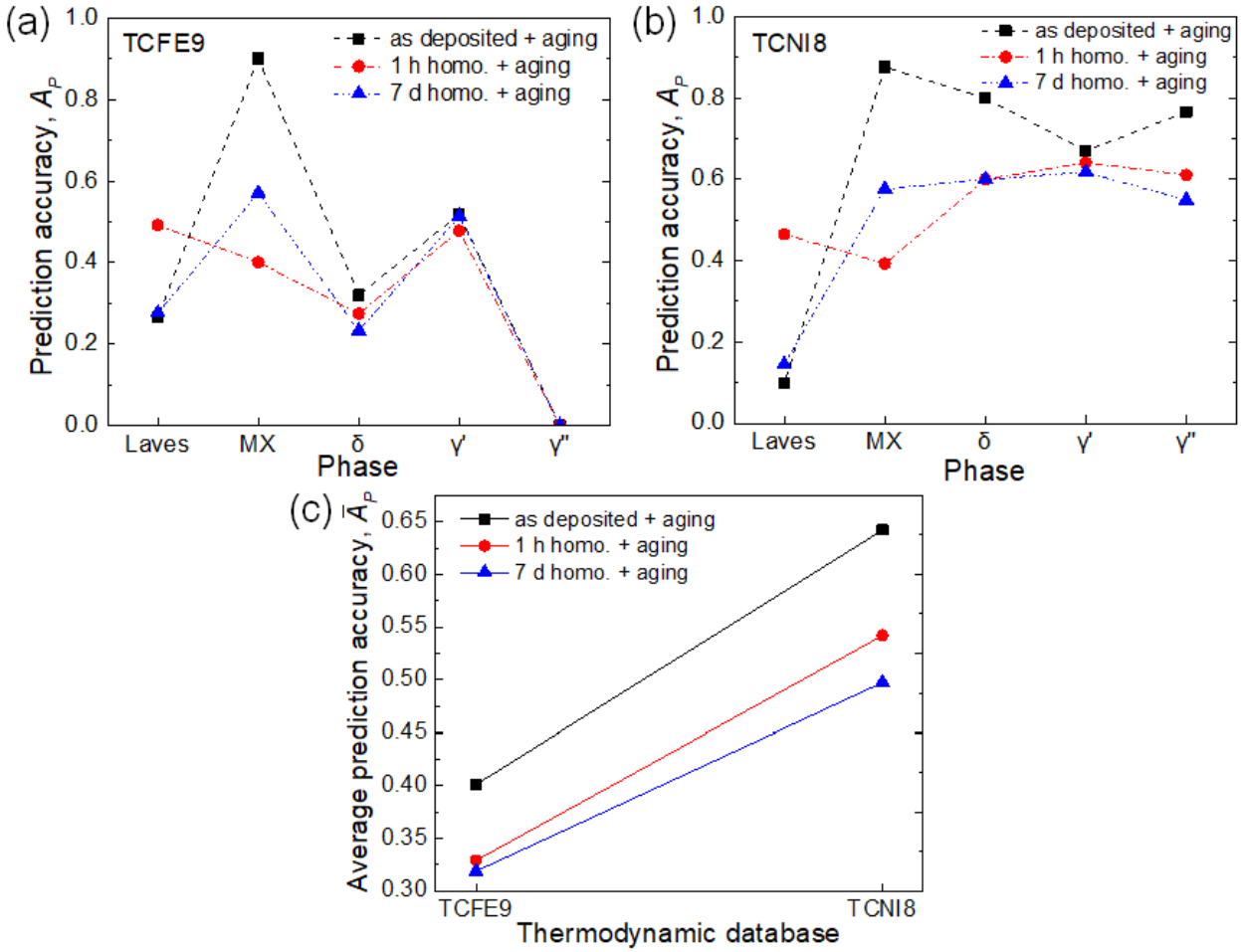

Figure 12. The evolutions of prediction accuracy A_P values under different simulation databases and thermodynamic conditions: (a) TCFE9 database, (b) TCNI8 database and (c) average prediction accuracy.3.4. Mechanical properties in FGMs and responds to post heat treatments

As the deposited size of the FGM is limited, the microhardness instead of tensile tests was conducted systematically to investigate the mechanical properties of the FGM samples with different homogenization and aging conditions. Figure 13 shows the hardness evolutions of different homogenized FGMs before and after aging. The as-deposited FGM has an obvious increase in hardness for each component as the weight percent of IN718 increases, with the increase from 200 Hv to 285 Hv (Fig. 13a). After 1 h homogenization, the jump of hardness between each component is reduced. When the FGM sample is homogenized for 7 d, the hardness change as a function of composition becomes very smooth. This is due to the smooth gradient of composition in the FGM after the long term of homogenization, as stated in Section 3.2.1. The increase in hardness is because of the increased MX precipitation with the weight percent of IN718 increasing. Moreover, as the homogenization time increases, the hardness decreases gradually. It is because the grain grows up significantly after homogenization (Figs. 5b and 5e). After the aging heat treatment at 718°C for 15 h, the hardness in the components with the composition from pure SS316 to pure IN718 has a very big difference (Fig. 13b), which is owing to the different precipitation in each component. For the "as-deposited+aging" FGM, the hardness has an obvious increase after the composition is higher than 25wt.% IN718, as indicated by point 1. This is because the precipitation in the interface region begins to transform from δ phase to γ′ and γ′′ phases, as the evidence showed in Fig. 8f. The γ′ and γ′′ phases have much more efficient strengthening contribution than the δ

Preprints (www.preprints.org) | NOT PEER-REVIEWED | Posted: 15 April 2022 doi:10.20944/preprints202204.0139.v1

phase. The differences on the volume fraction of γ′ and γ′′ phases in the components with 50wt.%, 75wt.% and 100wt.% IN718 also result in big difference on the hardness of each component in the as-deposited+aging sample.

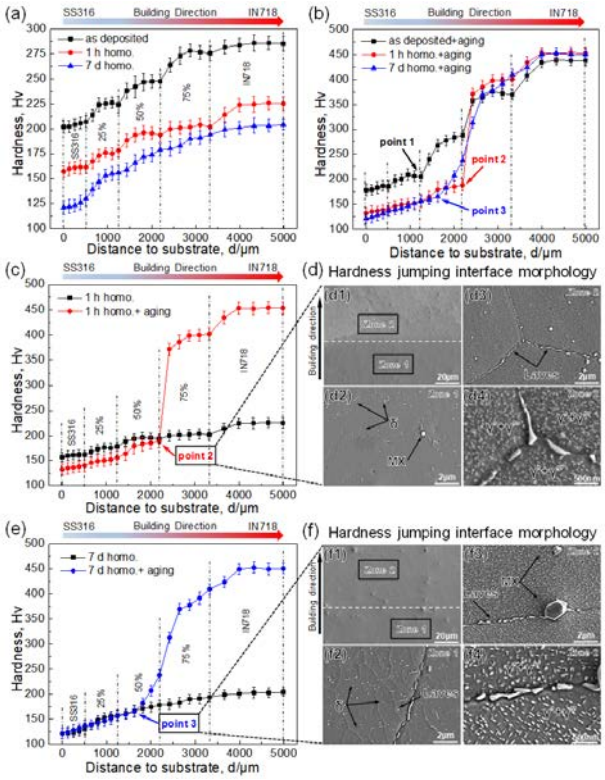

Figure 13. The hardness evolutions of different homogenized FGMs before (a) and after (b) aging heat treatment, (c) the hardness evolution with 1 h homogenization, (d) interface morphology in the hardness jumping zone of point 2 after aging, (e) the hardness evolution with 7 d homogenization and (f) interface morphology in the hardness jumping zone of point 3 after aging. ((d2) and (d3) are the magnified images of zone 1 and zone 2 in (d1), respectively, (d4) is the magnified image of (d3); (f2) and (f3) are the magnified images of zone 1 and zone 2 in (f1), respectively, (f4) is the magnified image of (f3)).

In comparison, the hardness of the "1 h homo.+aging" FGM has a remarkable jump at the interface between the components with 50wt.% and 75wt.%, as indicated by point 2. The zone of point 2 where the hardness jumps was observed under SEM, as presented in Fig. 13d. Thereinto, Fig. 13c further compares the significant hardness change before and after aging in the 1 h homogenized FGM sample, with the critical jumping point 2. It can be seen that there is a clear interface of precipitation in the zone of point 2 (Fig. 13d1). Beside the MX and Laves phases, there is plenty of δ phase in Zone 1 below the interface (Fig. 13d2), while there are tremendous γ′ and γ′′ nanoprecipitates in Zone 2 right above the interface (Figs. 13d3 and 13d4). This fact results in the big change of hardness near point 2. The similar phenomenon exists in the "7 d homo.+aging" FGM, as showed in Figs. 13e and 13f. However, the interface moves to point 3, which is furthermore down towards the steel side. The δ phase and γ′ and γ′′ phases become bigger in the zone below and above the interface, respectively (Figs. 13f2-13f4). In addition, the interface of precipitation is not as clear as that in the "1 h homo.+aging" FGM (Fig. 13f1). The hardness change becomes smooth as a function of composition of IN718. All of these results are attributed to the smooth compositional gradient after the long term of homogenization.

Comparing Figs. 13a and 13b, another interesting phenomenon worth to notice is that aging heat treatment has a significant influence on the hardness of the components near the IN718 superalloy side, while homogenization heat treatment has a significant influence on the hardness of the components near the SS316 steel side. This indicates that the precipitation strengthening is the dominant contribution to the mechanical properties

 doi:10.20944/preprints202204.0139.v1

for the Ni-based alloys because of the tremendous γ′ and γ′′ nanoprecipitates. Nevertheless, the grain-refinement strengthening is the dominant contribution to the mechanical properties for the steels, because there is no plenty of hardening precipitates in the components near the steel side. This causes their hardness decreases gradually after homogenization and aging heat treatments. In conclusion, the post heat treatments including homogenization and aging have compelling effects on the hardness and strengthening mechanisms, which can create compatible mechanical properties in the components of the FGM. They play a critical role in the gradient smoothing and microstructure-property improvement of the FGM fabrication.

4. Conclusions

In the present work, the functionally graded material (FGM) from 316 stainless steel to Inconel 718 is fabricated using the powder-based laser direct energy deposition (DED). The gradient microstructure and aging precipitation behaviors has been studied via experimental characterization and computation. The high-throughput thermodynamic modeling is exploited to evaluate the experimental microstructure and computational uncertainty using different thermodynamic conditions and databases. The main conclusions are summarized below:

(1) The FGM without cracks and distortions is successfully built using the laser DED fabrication method. The composition of this FGM from 316 stainless steel to Inconel 718 is well controlled using hybrid powder feed system.

(2) The 75wt.% IN718 component with fine and equiaxial grains is directly obtained from the laser deposition, which has a great potential for use in AM industry with the advantage of avoiding post heat treatments. It is found to have the highest entropy in all compositions. The FGM fabricated using laser DED method provide a high-throughput way to develop new high entropy alloys and functional alloys.

(3) The aging precipitation behaviors in the FGM from Fe-based alloy to Ni-based alloy are for the first time studied. The phase transformations in these gradient components with different compositions are elucidated in depth. The diffusion and segregation of Ni, Nb and Ti elements underly the transformation mechanism between Laves, δ, γ′ and γ′′ phases.

(4) Two thermodynamic databases of TCFE and TCNI on the prediction for alloys with the major elements of Fe and Ni are for the first time to be evaluated using the high-throughput thermodynamic modeling combined with the experimental results in the FGM. The TCNI databases has a much better phase prediction than TCFE databases for the alloys with the Ni content higher than 20wt.%.

(5) Homogenization has a significant utility on the gradient smoothening and microstructure-property improvement for the FGM. It can not only eliminate the heterogeneity inherited from the AM process, but also provide a practical way to smoothen the gradient on composition and microstructure for the eventual good gradient properties.

(6) Homogenization heat treatment has a direct influence on the following aging precipitation behaviors in the FGM, which highly relies on the diffusion degree of the elements in the matrix and grain boundaries.

(7) The uncertainty of thermodynamic modeling is evaluated via the hybrid high-throughput design on experiment and computation. Three thermodynamic conditions and simulation databases are used to quantify the prediction accuracy on different secondary phases, which addresses the uncertainty of thermodynamic modeling for further improvement in the future.

Acknowledgements and Notes on Authorship Contribution

This work related to heat treatment and microstructure analysis was performed when Kun Li was performing his postdoctoral research at the University of Pittsburgh in 2019-2020 under the supervision of Wei Xiong. Kun Li used the samples prepared in Wei Xiong's lab from 2017 to 2018, when a master student Yongshuo Jiang was learning depositing graded alloy through Optomec LENS® 450 printing system at the ANSYS Additive Manufacturing Laboratory. The research ideas were proposed by Wei Xiong, and thermodynamic modeling was performed by Xin Wang. The Thermo-Calc software license for this work is from Wei Xiong's research group. However, the manuscript was published unexpectedly in the TMS proceeding by Kun Li, *(Kun Li, Jianbin Zhan, Peng Jin, Qian Tang, David Z. Zhang, Wei Xiong, Huajun Cao (2022). Functionally Graded Alloys from 316 Stainless Steel to Inconel 718 by Powder-Based Laser Direct Energy Deposition. In: TMS 2022 151st Annual Meeting & Exhibition Supplemental Proceedings. The Minerals, Metals & Materials Series. Springer, Cham. https://doi.org/10.1007/978-3-030-92381-5_28. Wei Xiong was not aware of the submission until the manuscript was in-press for publication)*, Later this work was further released as *Kun Li, Jianbin Zhan, Ming Zhang, Ruijin Ma, Qian Tang, David Z. Zhang, Lawrence E. Murr, Huajun Cao, A functionally graded material design from stainless steel to Ni-based superalloy by laser metal deposition coupled with thermodynamic prediction, Materials & Design, 217 (2022) 110612.* https://doi.org/10.1016/j.matdes.2022.110612. on March 30, 2022. After observing these on April 14, 2022, by Wei Xiong, in order to clearly state the authorship contribution of this work, it is important to post the manuscript draft in this format as a preprint, although some results in this manuscript draft should be further refined. The manuscript draft was prepared by Kun Li in Summer, 2020 (before Kun Li left Pitt), with the help of Xin Wang on computation based on the conceptualization initiated by Wei Xiong. The present version of the manuscript draft has not been fully revised by all authors.

References

[1] C.D. Lundin, Dissimilar metal welds-transition joints literature review, Weld. J. 61 (1982) 58–63.

[2] D.I. Roberts, R.H. Ryder, R. Viswanathan, Performance of dissimilar welds in service, J. Press. Ves. 107 (1985) 247-254.

[3] C. Jang, J. Lee, J.S. Kim, T.E. Jin, Mechanical property variation within Inconel 82/182 dissimilar metal weld between low alloy steel and 316 stainless steel, Int. J. Press. Vessel. Pip. 85 (2008) 635–646.

[4] J.N. DuPont, Microstructural evolution and high temperature failure of ferritic to austenitic dissimilar welds, Int. Mater. Rev. 57 (2012) 208–234.

[5] G.J. Brentrup, B.S. Snowden, J.N. DuPont, J.L. Grenestedt, Design considerations of graded transition joints for welding dissimilar alloys, Weld. J. 91 (2012) 252–259.

[6] G.J. Brentrup, J.N. DuPont, Fabrication and characterization of graded transition joints for welding dissimilar alloys, Weld. J. 92 (2013) 72–79.

[7] D. Deng, K. Ogawa, S. Kiyoshima, N. Yanagida, K. Saito, Prediction of residual stresses in a dissimilar metal welded pipe with considering cladding, buttering and post weld heat treatment, Comput. Mater. Sci. 47 (2009) 398–408.

[8] M.K. Samal, M. Seidenfuss, E. Roos, K. Balani, Investigation of failure behavior of ferritic–austenitic type of dissimilar steel welded joints, Eng. Fail. Anal. 18 (2011) 999–1008.

[9] T.-K. Yeh, G.-R. Huang, M.-Y. Wang, C.-H. Tsai, Stress corrosion cracking in dissimilar metal welds with 304L stainless steel and Alloy 82 in high temperature water, Prog. Nucl. Energy. 63 (2013) 7–11.

[10] H.T. Wang, G.Z. Wang, F.Z. Xuan, S.T. Tu, Fracture mechanism of a dissimilar metal welded joint in nuclear power plant, Eng. Fail. Anal. 28 (2013) 134–148.

[11] Z. Zeng, X. Li, Y. Miao, G. Wu, Z. Zhao, Numerical and experiment analysis of residual stress on magnesium alloy and steel butt joint by hybrid laser-TIG welding, Comput. Mater. Sci. 50 (2011) 1763–1769.

[12] D. Delfosse, N. Cherradi, B. Ilschner, Numerical and experimental determination of residual stresses in graded materials, Compos. Part B Eng. 28 (1997) 127–141.

[13] D. Qiao, W. Zhang, T.-Y. Pan, P. Crooker, S. David, Z. Feng, Evaluation of residual plastic strain distribution in dissimilar metal weld by hardness mapping, Sci. Technol. Weld. Join. 18 (2013) 624–630.

[14] M. Sireesha, V. Shankar, S.K. Albert, S. Sundaresan, Microstructural features of dissimilar welds between 316LN austenitic stainless steel and alloy 800, Mater. Sci. Eng. A. 292 (2000) 74–82.

[15] V. Anes, R.S. Pedro, E. Henriques, M. Freitas, L. Reis, Galvanic corrosion of aircraft bonded joints as a result of adhesive microcracks, Procedia Struct. Integr. 1 (2016) 218–225.

[16] M. Koizumi, M. Niino, Overview of FGM research in Japan, Mrs Bull. 20 (1995) 19–21.

[17] A. Mortensen, S. Suresh, Functionally graded metals and metal-ceramic composites: Part 1 Processing, Int. Mater. Rev. 40 (1995) 239–265.

[18] V. Birman, Functionally graded materials and structures, Encycl. Therm. Stress. RB Hetnarski, Ed., Springer, Dordrecht, Netherlands. (2014) 1858–1864.

[19] S.K. Bohidar, R. Sharma, P.R. Mishra, Functionally graded materials: A critical review, Int. J. Res. 1 (2014) 289–301.

[20] Z. Liu, M.A. Meyers, Z. Zhang, R.O. Ritchie, Functional gradients and heterogeneities in biological materials: Design principles, functions, and bioinspired applications, Prog. Mater. Sci. 88 (2017) 467–498.

[21] T. Gebhardt, D. Music, T. Takahashi, J.M. Schneider, Combinatorial thin film materials science: From alloy discovery and optimization to alloy design, Thin Solid Films. 520 (2012) 5491–5499.

[22] E.A. Jägle, Small variations in powder composition lead to strong differences in part properties, in: Alloy. Addit. Manuf. Work. 2016, 2016.

[23] H. Knoll, S. Ocylok, A. Weisheit, H. Springer, E. Jägle, D. Raabe, Combinatorial alloy design by laser additive manufacturing, Steel Res. Int. 88 (2017) 1600416.

[24] W.Y. Lee, Y.W. Bae, K.L. More, Synthesis of functionally graded metal-ceramic microstructures by chemical vapor deposition, J. Mater. Res. 10 (1995) 3000–3002.

[25] K.A. Khor, Z.L. Dong, Y.W. Gu, Plasma sprayed functionally graded thermal barrier coatings, Mater. Lett. 38 (1999) 437–444.

[26] M.M. Nemat-Alla, M.H. Ata, M.R. Bayoumi, W. Khair-Eldeen, Powder metallurgical fabrication and microstructural investigations of aluminum/steel functionally graded material, Mater. Sci. Appl. 2 (2011) 1708.

[27] S. Suryakumar, M.A. Somashekara, Manufacture of functionally gradient materials using weld-deposition solid, in: Free. Fabr. Symp, 2013: pp. 1–36.

[28] Z.Y. Hang, M.E. Jones, G.W. Brady, R.J. Griffiths, D. Garcia, H.A. Rauch, C.D. Cox, N. Hardwick, Non-beam-based metal additive manufacturing enabled by additive friction stir deposition, Scr. Mater. 153 (2018) 122–130.

[29] Y. Watanabe, Y. Inaguma, H. Sato, E. Miura-Fujiwara, A novel fabrication method for functionally graded materials under centrifugal force: The centrifugal mixed-powder method, Materials (Basel). 2 (2009) 2510–2525.

[30] K.M. Jasim, R.D. Rawlings, D.R.F. West, Metal-ceramic functionally gradient material produced by laser processing, J. Mater. Sci. 28 (1993) 2820–2826.

[31] D.C. Hofmann, J. Kolodziejska, S. Roberts, R. Otis, R.P. Dillon, J.-O. Suh, Z.-K. Liu, J.-P. Borgonia, Compositionally graded metals: A new frontier of additive manufacturing, J. Mater. Res. 29 (2014) 1899–1910.

[32] C. Zhang, F. Chen, Z. Huang, M. Jia, G. Chen, Y. Ye, Y. Lin, W. Liu, B. Chen, Q. Shen, Additive manufacturing of functionally graded materials: A review, Mater. Sci. Eng. A. 764 (2019) 138209.

[33] A. Reichardt, A.A. Shapiro, R. Otis, R.P. Dillon, J.P. Borgonia, B.W. McEnerney, P. Hosemann, A.M. Beese, Advances in additive manufacturing of metal-based functionally graded materials, Int. Mater. Rev. (2020) 1–29.

[34] K.G. Prashanth, S. Scudino, T. Maity, J. Das, J. Eckert, Is the energy density a reliable parameter for materials synthesis by selective laser melting?, Mater. Res. Lett. 5 (2017) 386–390.

[35] S. Tammas-Williams, I. Todd, Design for additive manufacturing with site-specific properties in metals and alloys, Scr. Mater. 135 (2017) 105–110.

[36] A. Bandyopadhyay, B.V. Krishna, W. Xue, S. Bose, Application of laser engineered net shaping (LENS) to manufacture porous and functionally graded structures for load bearing implants, J. Mater. Sci. Mater. Med. 20 (2009) 29.

[37] D.D. Gu, W. Meiners, K. Wissenbach, R. Poprawe, Laser additive manufacturing of metallic components: materials, processes and mechanisms, Int. Mater. Rev. 57 (2012) 133–164.

[38] A. Hinojos, J. Mireles, A. Reichardt, P. Frigola, P. Hosemann, L.E. Murr, R.B. Wicker, Joining of Inconel 718 and 316 Stainless Steel using electron beam melting additive manufacturing technology, Mater. Des. 94 (2016) 17–27.

[39] S.M. Yusuf, N. Gao, Influence of energy density on metallurgy and properties in metal additive manufacturing, Mater. Sci. Technol. 33 (2017) 1269–1289.

[40] A. Reichardt, R.P. Dillon, J.P. Borgonia, A.A. Shapiro, B.W. McEnerney, T. Momose, P. Hosemann, Development and characterization of Ti-6Al-4V to 304L stainless steel gradient components fabricated with laser deposition additive manufacturing, Mater. Des. 104 (2016) 404–413.

[41] K. Shah, Laser direct metal deposition of dissimilar and functionally graded alloys, [Department of Mechanical Engineering]. Manchester: University of Manchester (2011) 220.

[42] S.R. Pulugurtha, Functionally graded Ti6Sl4V and Inconel 625 by laser metal deposition, [Materials Science and Engineering]. Missouri University of Science and Technology (2014) 220.

[43] I. Shishkovsky, F. Missemer, I. Smurov, Direct metal deposition of functional graded structures in Ti-Al system, Phys. Procedia. 39 (2012) 382–391.

[44] S.C. Deevi, V.K. Sikka, Nickel and iron aluminides: an overview on properties, processing, and applications, Intermetallics. 4 (1996) 357–375.

[45] S. Chen, J. Huang, J. Xia, H. Zhang, X. Zhao, Microstructural characteristics of a stainless steel/copper dissimilar joint made by laser welding, Metall. Mater. Trans. A. 44 (2013) 3690–3696.

[46] R. Banerjee, P.C. Collins, D. Bhattacharyya, S. Banerjee, H.L. Fraser, Microstructural evolution in laser deposited compositionally graded α/β titanium-vanadium alloys, Acta Mater. 51 (2003) 3277–3292.

[47] X. Lin, T.M. Yue, H.O. Yang, W.D. Huang, Microstructure and phase evolution in laser rapid forming of a functionally graded Ti–Rene88DT alloy, Acta Mater. 54 (2006) 1901–1915.

[48] D. Herzog, V. Seyda, E. Wycisk, C. Emmelmann, Additive manufacturing of metals, Acta Mater. 117 (2016) 371–392.

[49] M. Hayes, C.E. Thornton, S.J. Ibarra, Clad and dissimilar metals. In: O'Brien A, editor. Welding handbook, materials and applications, part 1. Miami (Florida): American Welding Society (2011) 393–450.

[50] S.R. Pulugurtha, J.W. Newkirk, F.W. Liou, H.-N. Chou, Functionally Graded Materials by Laser Metal Deposition, Proceedings of the 20th Annual International Solid Freeform Fabrication Symposium, Austin, TX (2009) pp. 454–469.

[51] Y.-J. Liang, X.-J. Tian, Y.-Y. Zhu, J. Li, H.-M. Wang, Compositional variation and microstructural evolution in laser additive manufactured Ti/Ti–6Al–2Zr–1Mo–1V graded structural material, Mater. Sci. Eng. A. 599 (2014) 242–246.

[52] J.T. Hofman, D.F. De Lange, B. Pathiraj, J. Meijer, FEM modeling and experimental verification for dilution control in laser cladding, J. Mater. Process. Technol. 211 (2011) 187–196.

[53] J.A. Self, D.K. Matlock, D.L. Olson, An evaluation of austenitic Fe-Mn-Ni weld metal for dissimilar metal welding, Weld. J. 63 (1984) 282s-288s.

[54] J.N. DuPont. Dilution in fusion welding. In: Lienert T, Siewert T, Babu S, editors. ASM handbook, volume 6A, welding

fundamentals and processes. Materials Park (Ohio): ASM International (2011) pp. 115–121.

[55] L.D. Bobbio, B. Bocklund, R. Otis, J.P. Borgonia, R.P. Dillon, A.A. Shapiro, B. McEnerney, Z.-K. Liu, A.M. Beese, Experimental analysis and thermodynamic calculations of an additively manufactured functionally graded material of V to Invar 36, J. Mater. Res. 33 (2018) 1642–1649.

[56] L.D. Bobbio, B. Bocklund, R. Otis, J.P. Borgonia, R.P. Dillon, A.A. Shapiro, B. McEnerney, Z.-K. Liu, A.M. Beese, Characterization of a functionally graded material of Ti-6Al-4V to 304L stainless steel with an intermediate V section, J. Alloys Compd. 742 (2018) 1031–1036.

[57] W. Li, S. Karnati, C. Kriewall, F. Liou, J. Newkirk, K.M.B. Taminger, W.J. Seufzer, Fabrication and characterization of a functionally graded material from Ti-6Al-4V to SS316 by laser metal deposition, Addit. Manuf. 14 (2017) 95–104.

[58] J. Zhang, Y. Zhang, W. Li, S. Karnati, F. Liou, J.W. Newkirk, Microstructure and properties of functionally graded materials Ti6Al4V/TiC fabricated by direct laser deposition, Rapid Prototyp. J. (2018).

[59] R.M. Mahamood, E.T. Akinlabi, Effect of laser power and powder flow rate on the wear resistance behaviour of laser metal deposited TiC/Ti6Al4 V composites, Mater. Today Proc. 2 (2015) 2679–2686.

[60] L.D. Bobbio, R.A. Otis, J.P. Borgonia, R.P. Dillon, A.A. Shapiro, Z.-K. Liu, A.M. Beese, Additive manufacturing of a functionally graded material from Ti-6Al-4V to Invar: Experimental characterization and thermodynamic calculations, Acta Mater. 127 (2017) 133–142.

[61] C. Schneider-Maunoury, L. Weiss, P. Acquier, D. Boisselier, P. Laheurte, Functionally graded Ti6Al4V-Mo alloy manufactured with DED-CLAD® process, Addit. Manuf. 17 (2017) 55–66.

[62] M.S. Domack, J.M. Baughman, Development of nickel-titanium graded composition components, Rapid Prototyp. J. (2005).

[63] W. Liu, J.N. DuPont, Fabrication of functionally graded TiC/Ti composites by laser engineered net shaping, Scr. Mater. 48 (2003) 1337–1342.

[64] J. Yao, Y. Ding, R. Liu, Q. Zhang, L. Wang, Wear and corrosion performance of laser-clad low-carbon high-molybdenum Stellite alloys, Opt. Laser Technol. 107 (2018) 32–45.

[65] A. Yakovlev, E. Trunova, D. Grevey, M. Pilloz, I. Smurov, Laser-assisted direct manufacturing of functionally graded 3D objects, Surf. Coatings Technol. 190 (2005) 15–24.

[66] K. Shah, I. ul Haq, A. Khan, S.A. Shah, M. Khan, A.J. Pinkerton, Parametric study of development of Inconel-steel functionally graded materials by laser direct metal deposition, Mater. Des. 54 (2014) 531–538.

[67] C.H. Zhang, H. Zhang, C.L. Wu, S. Zhang, Z.L. Sun, S.Y. Dong, Multi-layer functional graded stainless steel fabricated by laser melting deposition, Vacuum. 141 (2017) 181–187.

[68] D.-K. Kim, W. Woo, E.-Y. Kim, S.-H. Choi, Microstructure and mechanical characteristics of multi-layered materials composed of 316L stainless steel and ferritic steel produced by direct energy deposition, J. Alloys Compd. 774 (2019) 896–907.

[69] T. Durejko, M. Ziętala, W. Polkowski, T. Czujko, Thin wall tubes with Fe3Al/SS316L graded structure obtained by using laser engineered net shaping technology, Mater. Des. 63 (2014) 766–774.

[70] B.E. Carroll, R.A. Otis, J.P. Borgonia, J. Suh, R.P. Dillon, A.A. Shapiro, D.C. Hofmann, Z.-K. Liu, A.M. Beese, Functionally graded material of 304L stainless steel and inconel 625 fabricated by directed energy deposition: Characterization and thermodynamic modeling, Acta Mater. 108 (2016) 46–54.

[71] V.S. Babu, A.S. Pavlovic, M.S. Seehra, Oxidation characteristics and thermal expansion of inconel alloy 718 from 300 K to 1273 K, Superalloys 718, 625, 706 Var. Deriv. (1997) 689–693.

[72] K.N. Amato, S.M. Gaytan, L.E. Murr, E. Martinez, P.W. Shindo, J. Hernandez, S. Collins, F. Medina, Microstructures and mechanical behavior of Inconel 718 fabricated by selective laser melting, Acta Mater. 60 (2012) 2229–2239.

[73] T. Amine, J.W. Newkirk, F. Liou, An investigation of the effect of laser deposition parameters on characteristics of multilayered 316 L deposits, Int. J. Adv. Manuf. Technol. 73 (2014) 1739–1749.

[74] X. Lin, T.M. Yue, Phase formation and microstructure evolution in laser rapid forming of graded SS316L/Rene88DT alloy, Mater. Sci. Eng. A. 402 (2005) 294–306.

[75] P.L. Blackwell, The mechanical and microstructural characteristics of laser-deposited IN718, J. Mater. Process. Technol. 170 (2005) 240–246.

[76] K. Dai, L. Shaw, Distortion minimization of laser-processed components through control of laser scanning patterns, Rapid Prototyp. J. (2002).

[77] A. Yadollahi, N. Shamsaei, S.M. Thompson, D.W. Seely, Effects of process time interval and heat treatment on the mechanical and microstructural properties of direct laser deposited 316L stainless steel, Mater. Sci. Eng. A. 644 (2015) 171–183.

[78] H. Qi, M. Azer, A. Ritter, Studies of standard heat treatment effects on microstructure and mechanical properties of laser net shape manufactured Inconel 718, Metall. Mater. Trans. A. 40 (2009) 2410–2422.

[79] C. Qiu, N.J.E. Adkins, M.M. Attallah, Microstructure and tensile properties of selectively laser-melted and of HIPed laser-melted Ti–6Al–4V, Mater. Sci. Eng. A. 578 (2013) 230–239.

[80] J.-O. Andersson, T. Helander, L. Höglund, P. Shi, B. Sundman, Thermo-Calc & DICTRA, computational tools for materials science, Calphad. 26 (2002) 273–312.

[81] B. Sundman, B. Jansson, J.-O. Andersson, The thermo-calc databank system, Calphad. 9 (1985) 153–190.

[82] G.F. Albrecht, S.B. Sutton, E. V George, W.R. Sooy, W.F. Krupke, Solid state heat capacity disk laser, Laser Part. Beams. 16 (1998) 605–625.

[83] H.M. Künzel, K. Kiessl, Calculation of heat and moisture transfer in exposed building components, Int. J. Heat Mass Transf. 40 (1996) 159–167.

[84] W.S. Fann, R. Storz, H.W.K. Tom, J. Bokor, Direct measurement of nonequilibrium electron-energy distributions in subpicosecond laser-heated gold films, Phys. Rev. Lett. 68 (1992) 2834.

[85] B.G. Muralidharan, V. Shankar, T.P.S. Gill, Weldability of Inconel 718-A review, Indira Gandhi Centre for Atomic Research, 1996.

[86] J.K. Hong, J.H. Park, N.K. Park, I.S. Eom, M.B. Kim, C.Y. Kang, Microstructures and mechanical properties of Inconel 718 welds by CO2 laser welding, J. Mater. Process. Technol. 201 (2008) 515–520.

[87] R.I.L. Guthrie, T. Iida, The physical properties of liquid metals, Clarendon press, 1987.

[88] L. Battezzati, A.L. Greer, The viscosity of liquid metals and alloys, Acta Metall. 37 (1989) 1791–1802.

[89] R.F. Brooks, A.T. Dinsdale, P.N. Quested, The measurement of viscosity of alloys - A review of methods, data and models, Meas. Sci. Technol. 16 (2005) 354–362.

[90] D.B. Miracle, O.N. Senkov, A critical review of high entropy alloys and related concepts, Acta Mater. 122 (2017) 448–511.

[91] Y.Y. Chen, T. Duval, U.D. Hung, J.W. Yeh, H.C. Shih, Microstructure and electrochemical properties of high entropy alloys—a comparison with type-304 stainless steel, Corros. Sci. 47 (2005) 2257–2279.

[92] K.B. Zhang, Z.Y. Fu, J.Y. Zhang, W.M. Wang, H. Wang, Y.C. Wang, Q.J. Zhang, J. Shi, Microstructure and mechanical properties of CoCrFeNiTiAlx high-entropy alloys, Mater. Sci. Eng. A. 508 (2009) 214–219.

[93] W.H. Liu, Y. Wu, J.Y. He, T.G. Nieh, Z.P. Lu, Grain growth and the Hall–Petch relationship in a high-entropy FeCrNiCoMn alloy, Scr. Mater. 68 (2013) 526–529.

[94] R. Sun, L. Li, Y. Zhu, W. Guo, P. Peng, B. Cong, J. Sun, Z. Che, B. Li, C. Guo, Microstructure, residual stress and tensile properties control of wire-arc additive manufactured 2319 aluminum alloy with laser shock peening, J. Alloys Compd.

747 (2018) 255–265.

[95] J. Michler, M. Mermoux, Y. Von Kaenel, A. Haouni, G. Lucazeau, E. Blank, Residual stress in diamond films: origins and modelling, Thin Solid Films. 357 (1999) 189–201.

[96] M. Winning, G. Gottstein, L.S. Shvindlerman, Stress induced grain boundary motion, Acta Mater. 49 (2001) 211–219.

[97] C.A. Powell-Doğan, A.H. Heuer, M.J. Ready, K. Merriam, Residual-stress-induced grain pullout in a 96% alumina, J. Am. Ceram. Soc. 74 (1991) 646–649.

[98] P. Feltham, Grain growth in metals, Acta Metall. 5 (1957) 97–105.

[99] D.A. Porter, K.E. Easterling, Phase transformations in metals and alloys, CRC press, 2009, 133-143.

[100] B.-N. Kim, K. Hiraga, K. Morita, Kinetics of normal grain growth depending on the size distribution of small grains, Mater. Trans. 44 (2003) 2239–2244.

[101] S. Jothi, T.N. Croft, L. Wright, A. Turnbull, S.G.R. Brown, Multi-phase modelling of intergranular hydrogen segregation/trapping for hydrogen embrittlement, Int. J. Hydrogen Energy. 40 (2015) 15105–15123.

[102] J. Yao, S.A. Meguid, J.R. Cahoon, Hydrogen diffusion and its relevance to intergranular cracking in nickel, Metall. Trans. A. 24 (1993) 105–112.

[103] E.G. Wagenhuber, V.B. Trindade, U. Krupp, The role of oxygen-grain-boundary diffusion during intercrystalline oxidation and intergranular fatigue crack propagation in alloy 718, in: Proc. Int. Symp. Superalloys Var. Deriv. Pittsburgh, PA, 2005.

[104] M.C. Chaturvedi, Y. Han, Strengthening mechanisms in Inconel 718 superalloy, Met. Sci. 17 (1983) 145–149.

[105] C. Slama, M. Abdellaoui, Structural characterization of the aged Inconel 718, J. Alloys Compd. 306 (2000) 277–284.

[106] Y. Zhao, K. Li, M. Gargani, W. Xiong, A Comparative Analysis of Inconel 718 Made by Additive Manufacturing and Suction Casting: Microstructure Evolution in Homogenization, Addit. Manuf., 2020. Submitted for publication.

[107] Y. Zhao, K. Li, F. Meng, S. Tan, W. Xiong, Variation of Process-structure-property relationships of additively manufactured Inconel 718 influenced by homogenization, Mater. Sci. Eng. A, 2020, Unpublished.

[108] Y. Zhao, N. Sargent, K. Li, W. Xiong, A new high-throughput method using additive manufacturing for materials design and processing optimization, Materilia, 2020. Submitted for publication.

[109] D.F. Paulonis, J.M. Oblak, D.S. Duvall, Precipitation in nickel-base alloy 718, Pratt and Whitney Aircraft, Middletown, Conn., 1969.

[110] A. Devaux, L. Nazé, R. Molins, A. Pineau, A. Organista, J.Y. Guédou, J.F. Uginet, P. Héritier, Gamma double prime precipitation kinetic in Alloy 718, Mater. Sci. Eng. A. 486 (2008) 117–122.

[111] P. Honarmandi, T.C. Duong, S.F. Ghoreishi, D. Allaire, R. Arroyave, Bayesian uncertainty quantification and information fusion in CALPHAD-based thermodynamic modeling, Acta Mater. 164 (2019) 636–647.

[112] R.A. Otis, Z.-K. Liu, High-throughput thermodynamic modeling and uncertainty quantification for ICME, JOM. 69 (2017) 886–892.

[113] H.N. Najm, B.J. Debusschere, Y.M. Marzouk, S. Widmer, O.P. Le Maître, Uncertainty quantification in chemical systems, Int. J. Numer. Methods Eng. 80 (2009) 789–814.